SUNSTORM 1/X-ray Flux Monitor for CubeSats (XFM-CS) : Instrument characterization and first results

Lehtolainen, A.

2022-07-11

Lehtolainen , A , Huovelin , J , Korpela , S , Kilpua , E , Andersson , H , Giurisato , D , Lehti , J , Saari , J , Peltonen , J , Säntti , T , Hirvonen , M , Talvioja , M , Luntama , T , Kuhno , J & Solin , O 2022 , ' SUNSTORM 1/X-ray Flux Monitor for CubeSats (XFM-CS) : Instrument characterization and first results ' , Nuclear Instruments & Methods in Physics Research. Section A: Accelerators, Spectrometers, Detectors, and Associated Equipment , vol. 1035 , 166865 . https://doi.org/10.1016/j.nima.2022.166865

http://hdl.handle.net/10138/348137
https://doi.org/10.1016/j.nima.2022.166865

Nuclear Inst. and Methods in Physics Research, A 1035 (2022) 166865

Contents lists available at ScienceDirect

Nuclear Inst. and Methods in Physics Research, A

journal homepage: www.elsevier.com/locate/nima

SUNSTORM 1/X-ray Flux Monitor for CubeSats (XFM-CS): Instrument characterization and first results

A. Lehtolainen [a,b,*], J. Huovelin [a,b], S. Korpela [a,b], E. Kilpua [a], H. Andersson [c], D. Giurisato [c], J. Lehti [d], J. Saari [d], J. Peltonen [d], T. Säntti [d], M. Hirvonen [d], M. Talvioja [e], T. Luntama [b], J. Kuhno [f], O. Solin [b,a]

[a] Department of Physics, University of Helsinki, Helsinki, P.O. Box 48, FI 00014, Finland
[b] Isaware Oy, Dynamicum, Erik Palmenin Aukio 1, 00560 Helsinki, Finland
[c] Oxford Instruments Technologies Oy, Technopolis Innopoli 1, Tekniikantie 12, 02150 Espoo, Finland
[d] Aboa Space Research Oy, Tierankatu 4B, 20520 Turku, Finland
[e] Talvioja Consulting Oy, Omenamäenkatu 9, 00990 Helsinki, Finland
[f] Kuva Space Oy, Otakaari 5/A Grid, 02150 Espoo, Finland

ARTICLE INFO

Keywords:
Solar X-rays
Solar corona
Space weather
Silicon drift detector
Characterization
In-orbit demonstration

ABSTRACT

SUNSTORM 1 CubeSat was launched to Sun-synchronous low Earth orbit on August 17 2021. The primary purpose of the mission is an in-orbit demonstration of X-ray Flux Monitor (XFM) instrument. XFM is an innovative solar X-ray spectrometer for measuring and characterizing solar flares, which are known to be linked to a variety of space weather phenomena. XFM represents a next generation of solar X-ray flux monitors. It is based on silicon drift detector technology, which provides several notable performance improvements over its predecessors, which are based on Si PIN detectors. Transversal electric field and lower output capacitance allow operation at much faster pulse processing shaping times, allowing the system to achieve about 10 times higher throughput without saturation while also making it less sensitive to the increase of leakage current due to high temperature and/or radiation damage. Thus, XFM instruments can cover a very wide dynamic range of solar X-ray emission from the most quiescent conditions to the strongest X-class solar flares, while maintaining good spectral resolution (<200 eV at 6 keV). The instruments are thus well suited for both X-ray flux monitoring and spectroscopic studies of the solar corona.

In this paper we describe the ground characterization and evaluation of the scientific performance of the first operational XFM instrument, a CubeSat version XFM-CS on-board SUNSTORM 1, which is a satellite built in the framework of the FLY element of ESA's General Support Technology Programme, dedicated to the early space testing of promising new technologies. We also provide an analysis of the first results obtained during the in-orbit commissioning and early operations of SUNSTORM 1. We show the comparison of the observed scientific performance of XFM-CS with the expected performance based on theoretical modeling and ground calibration results. Finally, we describe the cross calibration of the X-ray flux data from XFM-CS with the new GOES-R series GOES X-ray sensors.

1. Introduction

SUNSTORM 1 is a 2-unit CubeSat that was launched by ESA to Sun-synchronous low Earth orbit (LEO) with an altitude of 551 km on August 17 2021. An artist's rendition of the satellite in space is shown in Fig. 1 (left). The payload is X-ray Flux Monitor for CubeSats (XFM-CS), an innovative solar X-ray spectrometer (Fig. 1 right) for measuring and characterizing solar flares, which are known to cause a variety of space weather phenomena and are related to solar energetic particle (SEP) events, and may be accompanied by coronal mass ejections (CME). These affect the functionality of electronic devices and technological systems both in space and on ground, and can, in the worst case, shut off satellites, cause blackouts of long range radio frequency communication, and destroy electric power grids. The high energy particles associated with SEP events can also endanger the health of astronauts in space, and penetrate to the upper atmosphere affecting its chemistry and dynamics, and enhancing the radiation dose of the passengers and crew in airplanes flying over the polar regions.

Since solar X-rays are absorbed effectively by the Earth's atmosphere, they must be observed from space. Currently most of our data about solar X-rays comes from the Geostationary Operational Environmental Satellites (GOES) operated by the National Oceanic and

* Corresponding author at: Department of Physics, University of Helsinki, Helsinki, P.O. Box 48, FI 00014, Finland.
E-mail address: arto.lehtolainen@helsinki.fi (A. Lehtolainen).

https://doi.org/10.1016/j.nima.2022.166865
Received 14 March 2022; Received in revised form 14 April 2022; Accepted 10 May 2022
Available online 21 May 2022

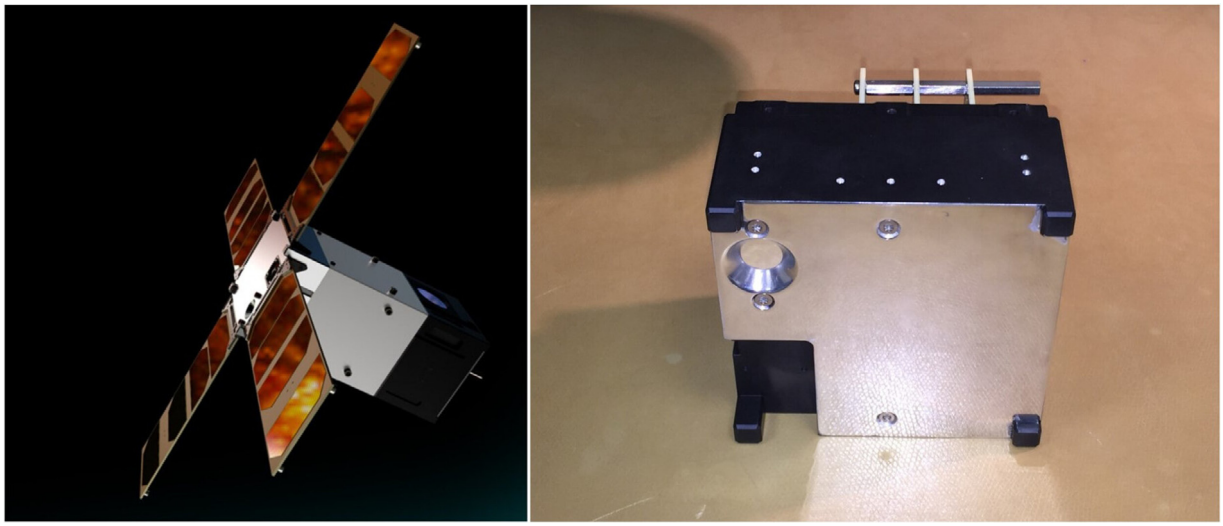

Fig. 1. Left: Artist's impression of SUNSTORM 1 CubeSat in space. XFM-CS instrument unit (figure on the right) is in the left part of the CubeSat with solar panels attached by hinges on the corners of the front and side panels. The collimator of the instrument and the Sun sensor of the CubeSat are facing to the left (Courtesy of Kuva Space Oy.). Right: XFM-CS instrument before integration with the CubeSat.

Atmospheric Administration (NOAA) of the USA. The primary purpose of the SUNSTORM 1 mission is in-orbit demonstration of the XFM instrument. The instrument is based on solid state detector and has much higher energy resolution than the GOES-R series GOES X-ray detectors. This allows collection of more information on solar X-rays as high resolution spectral data, in addition to the standard broadband flux data. A CubeSat mission at low Earth orbit is an efficient way for demonstration and testing of new technologies in space before their application in larger space missions at higher orbits.

The design of XFM-CS has heritage on the Solar X-ray Spectrometers (XSM) flown on-board ESA's SMART-1 mission and ISRO's Chandrayaan-1 mission, as well as the X-ray detector system of the Solar Intensity X-ray and particle Spectrometer (SIXS) on-board ESA's and JAXA's BepiColombo mission to Mercury. A review of the performance and first results of the SMART-1 XSM is presented in [1] and a study of cross calibrations with GOES X-ray detectors as well as Reuven Ramaty High Energy Solar Spectroscopic Imager (RHESSI: [2]) was performed by Väänänen et al. in 2009 [3]. The performance evaluation and characterization of the Chandrayaan-1 XSM was performed by Alha et al. in 2009 [4], and the data obtained with it was used e.g. in the investigation of elemental abundances of the solar corona [5] and the changes in first ionization potential (FIP) bias during the evolution of flares [6]. The instrument design and first results of SIXS were published by Huovelin et al. [7]. The similarities of XFM-CS with the heritage instruments are mostly in the logic of pre-processing of science data and in the baseline data products, as well as in the design of the detector package. However, the X-ray detector chip itself is based on Silicon Drift Detector (SDD) technology unlike the detectors of the heritage instruments, which are based on Si PIN detectors. The use of SDD technology provides several notable performance improvements over the heritage instruments. Coupled with new electronics design this enables much faster pulse processing. This allows an SDD detector to achieve about 10 times higher throughput with low pile-up than an Si PIN detector. In addition, operating at faster shaping time also makes the system significantly less sensitive to the increase of leakage current at high temperature or increased radiation damage. Thus, XFM can be operated and maintain good energy resolution in a very wide temperature range up to normal room temperature. This also means that lower power is needed for cooling of the detector chip and helps reducing the overall power required for the operation of the XFM instrument.

The SUNSTORM 1 S/C is three axis stabilized in such a way that the panel with XFM detector aperture/collimator is pointing continuously towards the Sun. In order to avoid light from the Earth's atmosphere and to minimize the sky background, XFM-CS has an aluminum collimator in front of its entrance window, limiting its field-of-view (FoV) into a cone with 10° angular diameter. This differs significantly from the heritage instruments, which have a wide, about 100° FoV for individual detectors, enabling observations of the Sun within a large range of S/C attitudes. A further benefit from the aluminum collimator is that it provides effective additional radiation shielding for the detector.

In this paper we describe the characterization and evaluation of scientific performance of the XFM-CS instrument. The ground calibration of the instrument was performed during the period September 21 to October 6 2020. We also provide an analysis of the first results of observations made with SUNSTORM 1/XFM-CS during the in-orbit commissioning and early observations. We compare the observed scientific performance of XFM-CS with the expected performance and ground calibration results. Finally, we perform a cross calibration of the X-ray flux data from XFM-CS with GOES-16 and GOES-17 X-ray flux data.

2. Instrument description

2.1. Scientific requirements

The requirements of the XFM instruments are based on the need for detecting solar X-ray flares, which are one of the most significant phenomena on the Sun giving rise to space weather phenomena in the heliosphere up to the Earth's distance and beyond. The standard scale of solar X-ray activity and solar flares is based on measurements of the X-ray emission of the entire visible disk of the Sun, including the solar corona, simultaneously in two X-ray wavelength bands, GOES long 1–8 Å(1.55 –12.4 keV), and GOES short 0.5–4 Å(3.1–24.8 keV). Such measurements yield directly values of the physical X-ray flux of the Sun in a common intensity scale of flare intensity from A2 ($2 \cdot 10^{-8}$ W/m^2) to X20 ($2 \cdot 10^{-3}$ W/m^2). This scale refers to flux values in the GOES long wavelength band.

The FoV of XFM instruments must be such that it covers the Sun continuously, including the corona, taking into account the pointing accuracy and stability of the S/C. Since SUNSTORM 1 is three-axis stabilized vs. the Sun, the angular diameter of the FoV of XFM-CS is designed to be only 10° to avoid/minimize the contamination of the signal from the Sun by radiation from the Earth and its atmosphere. The energy range of the XFM instruments must cover both GOES wavelength bands and the energy resolution must be such that the

physical X-ray fluxes in each band can be determined accurately. In practice, the GOES X-ray solar sensors have reduced sensitivity down to < 1 keV energies [8], and it is useful to extend the range of XFM-CS as well, to be able to determine with high accuracy the solar X-ray emission down to the lower limit of the GOES sensitivity. Therefore, XFM-CS includes a separate low energy band 1.0–1.55 keV for this extension below the nominal GOES long X-ray band. The target for dynamic range of the XFM-CS instrument was that it covers the flare intensity scale from B2 to X10.

A typical rise time of a flare is a few tens of seconds to minutes, while the decay is much longer, from tens of minutes up to hours for very large flares. The timescale of the rise of flares, and the need for an alert as soon as a significant increase of the flux is observed, giving a reliable indication of the rise of a flare, are the defining factors for the time resolution and measurement cadence requirements of the XFM instruments. The time resolution is 1 s for the X-ray flux data and 60 s for the high-resolution spectral data. The time resolution and the dynamic range of the XFM-CS are based on ESA requirements.

In addition to monitoring intensity variations of solar X-ray emission, XFM instruments are designed for spectroscopic studies of solar X-ray emission, and especially solar flares. The goal is in understanding better the physical processes giving rise to solar X-ray emission, being able to predict them and in improving our understanding of their association with CMEs, SEP events, and the full space weather chain. Getting forward in this task will require statistical studies of flare spectra and their relation with the physical dimensions and dynamical properties of individual flares, as well as the pre-eruptive structures within the solar corona, and most importantly for space weather forecasting, to get better understanding of the relationship between the characteristics X-ray spectra of flares and the space weather phenomena and their consequences at Earth. This motivates combining observations of XFM instruments with those of the Solar Dynamics Observatory [9], Solar Orbiter [10], and other space weather missions. Our experience indicates that for separation of important emission lines (ionized Mg, Al, Si, S, Ar, Ca, Fe, Ni, etc.) in the spectrum, energy resolution better than 400 eV (FWHM) at 6 keV is required. This value is the upper limit of energy resolution for the whole mission, i.e. End-of-Life (EOL). Since the energy resolutions of all solid state detectors degrade slowly under long time exposure to the radiation in space, the beginning-of-life (BOL) energy resolution of the XFM must be significantly better. How much better depends on the expected total dose during the mission, which, in turn, depends on the mission lifetime, and the radiation environment in its orbit.

The high-level scientific performance requirements for XFM instruments have been compiled in Table 1. Even with the very high throughput offered by SDD detector technology, XFM with a single detector cannot cover the whole range of flare intensity scale from A2 to X20, which is the range required from the XFM onboard future operative space weather missions. Therefore, the dynamic range requirement for XFM-CS was relaxed to flare intensity levels from B2 ($2 \cdot 10^{-7}$ W/m^2) to X10 ($1 \cdot 10^{-3}$ W/m^2). A version of XFM for upcoming space weather missions, whose dynamic range covers the whole intensity scale from A2 to X20 levels and beyond will include two simultaneously operating SDD detectors with different effective areas, which are dictated by the sizes of the circular apertures of the detectors. The use of two nearly identical detectors also provides redundancy and allows the instrument to maintain continuous observations (with limited dynamic range) even during periodic annealing of the detectors since the observations can continue with one detector while the other is being annealed.

2.2. Detector and collimator system

The detector of the XFM-CS is an SDD, which converts the photon energy to electrical charge by photoelectric absorption, the same physical phenomenon as the Si PIN technology used in the heritage instruments. A transverse electric field inside the detector chip will drift the charges to the P (holes) and N (electrons) junctions. The generated charge is conducted from the detector electrodes to an amplifier chain. Due to lower output capacitance of the SDD sensor it has lower noise at any particular combination of temperature and shaping time than Si PIN sensors. This allows operation with much faster pulse processor shaping times, and together with pulse processing in digital domain (Section 2.3) allows the system to achieve an order of magnitude higher throughput than with Si PIN. Additionally, operating at faster shaping time makes the increase of shot noise from leakage current due to high temperature and/or radiation damage smaller.

As mentioned above (see Introduction), the FoV of XFM-CS detector is limited by an aluminum collimator in order to minimize background signal from the Earth, Moon and other X-ray sources in the sky. Its inner surface is plated with Au to avoid contamination of the signal by fluorescence radiation from Al. The collimator also acts as a radiation shield for the detector. A schematic representation of the detector and collimator system is shown in Fig. 2 (left). The detector package itself is very similar to those of the heritage instruments SMART-1 XSM [1], Chandrayaan-1 XSM [4] and BepiColombo SIXS X-ray detectors [7]. The SDD is hermetically packaged with the preamplifier front-end components and a Peltier cooler inside a steel cup with a Be entrance window as a filter. An exploded view image of the detector package is shown in Fig. 2 (right). In front of the SDD there is an Au aperture that limits the effective area of the detector. Another advantage of the use of SDD detectors is that, due to the low noise and fast shaping time, they can be operated and maintain a good spectral resolution at normal room temperature (about +20 °C). They therefore require lower cooling power in the normal thermal conditions at distance of the Earth from the Sun, which significantly reduces the power consumption of the instrument. The Peltier cooler in XFM-CS is used mainly for stabilization of the temperature during normal operations and annealing of the detector chip.

The dimensions of the SDD and the filters were optimized based on the scientific performance requirements described in Section 2.1. In particular, SMART-1 XSM observations of solar flares of different intensities were used to create a simplified spectral model of solar X-rays that is based on bremsstrahlung continuum. The model was then extrapolated beyond the dynamic range of SMART-1 XSM and used to optimize the detector and filter dimensions by calculating the theoretical count rates that the modeled flares would produce when observed with XFM-CS detector. This was done by multiplying the model spectra with the effective area of the detector derived from the measured aperture size and dimensions and material information of filters and detector from the manufacturer (see Section 3.1). Dimensions were optimized so that the theoretical count rate would be high enough to produce sufficiently high signal to noise ratio (S/N) in order to enable reliable spectrum analysis at flare intensity level B2, but also remain below 6% pile-up of the instrument below flare intensity level X10.

The lower limit of a detector's dynamic range is determined by the lowest S/N, with which sufficiently accurate analysis of the spectrum is possible. Based on our experience with the XSM instruments used in SMART-1 and Chandrayaan-1 missions, we estimate that reliable spectral analysis is possible with a minimum number of total counts N ~200. With 60 s spectrum integration time this corresponds to count rate $I = 3.33$ counts per second (cps). Upper limit of the dynamic range is limited by the pile-up. Based on our experience with the XSM instruments, we estimate that the upper limit of pile-up in a spectrum that can be reliably analyzed is ~6%. The practical upper limit of the dynamic range is therefore the highest photon flux, where < 6% of the events are piled up. Pile-up occurs if the time interval between two successive photons is shorter than the pulse pair resolution time τ_p. The probability of pile-up occurring can be calculated for any total count rate I by applying Poisson statistics:

$$P_{pile-up} = \sum_n \frac{(\tau_p I)^n e^{-\tau_p I}}{n!} \quad (1)$$

Table 1
High level scientific performance requirements of XFM instruments.

Parameter	XFM	XFM-CS
Photon flux range	$2{\cdot}10^{-8}$ - $2{\cdot}10^{-3}$ W/m^{-2} (A2 - X20)	$2{\cdot}10^{-7}$ - $1{\cdot}10^{-3}$ W/m^{2} (B2 - X10)
Spectral Range	1.55–24.8 keV (requirement) 1–30 keV (design)	same as XFM
Spectral resolution	Flux: 6 channels 1–1.55 keV 1.55–3.1 keV 3.1–6.2 keV 6.2–12.4 keV 12.4–24.8 keV 24.8 keV–30 keV Spectrum: < 400 eV @ 6 keV (End of Life)	Same as XFM
Time resolution	1 s (flux) 60 s (spectrum)	same as XFM
Maximum count rate	300 000 cps (for each of 2 detectors)	300 000 cps
Field-of-View	10° angular diameter (scientific)	same as XFM
Aperture size	Detector 1: 0.3 ± 0.1 mm diameter Detector 2: 1.4 ± 0.1 mm diameter	0.6 ± 0.1 mm diameter
Background	< 1 cps per detector	< 1 cps
Linearity of spectrum histogram	< 10%	same as XFM

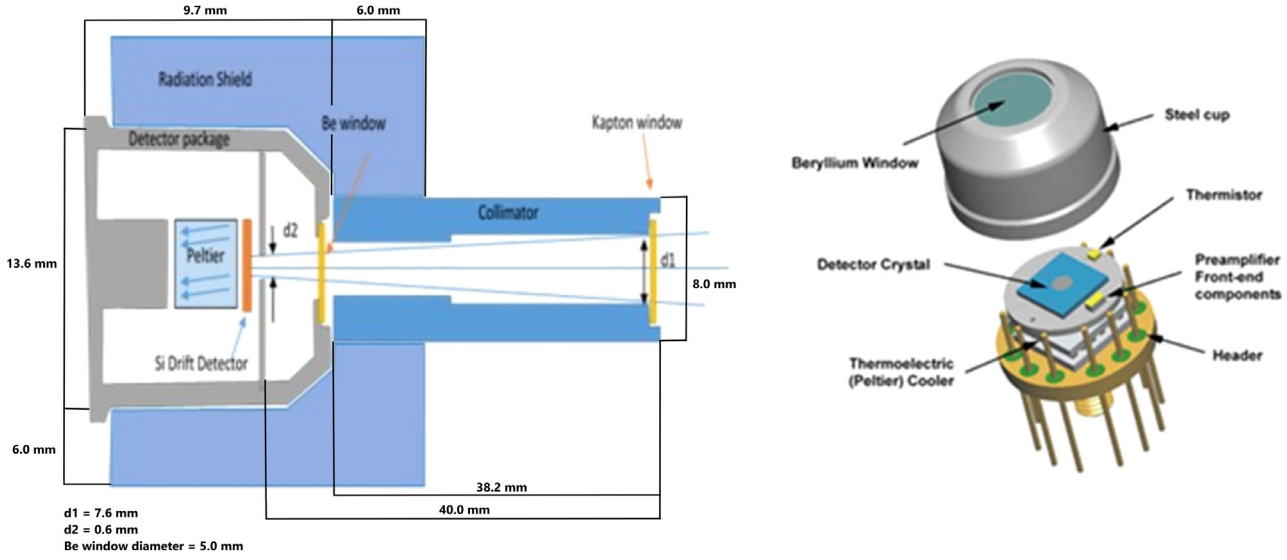

Fig. 2. Schematic representation of the detector and collimator system (left) and an exploded view of the detector package (right). The detector package looks similar to the X-ray detector package of the SIXS instrument on BepiColombo [7] and those of the XSM instruments flown on SMART-1 [1] and Chandrayaan1 [4] using Si PIN detectors. Similar Si PIN detector was also used on Messenger's solar X-ray monitor [11].

where n is the number of adjacent photons stacked together (piled up). The theoretical pulse pair resolution time of XFM-CS according to the manufacturers of the detector and the read-out electronics is 200 ns. Solving for I we get the practical upper limit of the count rate $I \approx$ 300000 cps. The dimensions of the detector and filters were therefore optimized so that 3.33 cps $< I <$ 300000 cps throughout the whole flare intensity range between B2 and X10 levels. The chosen values are shown in Table 2.

Table 2
Nominal dimensions of XFM-CS detector and filters.

Name	Value
Aperture size	Ø 0.6 mm
Scientific Field of View angular diameter	10°
Si drift detector thickness	450 μm
Inactive Si equivalent layer on surface	100 nm
Be window thickness	13 μm
Al on Be window surface	100 nm
Outer Kapton window thickness	7 μm
Al on Kapton surface	100 nm

2.3. Electronics

High-level functional diagram of XFM-CS is presented in Fig. 3. Photons absorbed within the SDD create current pulses that are led into the preamplifier. If the pulse height is above the detection threshold, pulse height analysis is triggered, resulting in a detection of the photon. In XFM-CS, A/D conversion is applied directly after the preamplifier, and actual pulse filtering, detection and pulse height analysis are implemented with digital signal processing. The pulse processing in digital domain allows the use of efficient methods like trapezoidal shaping and

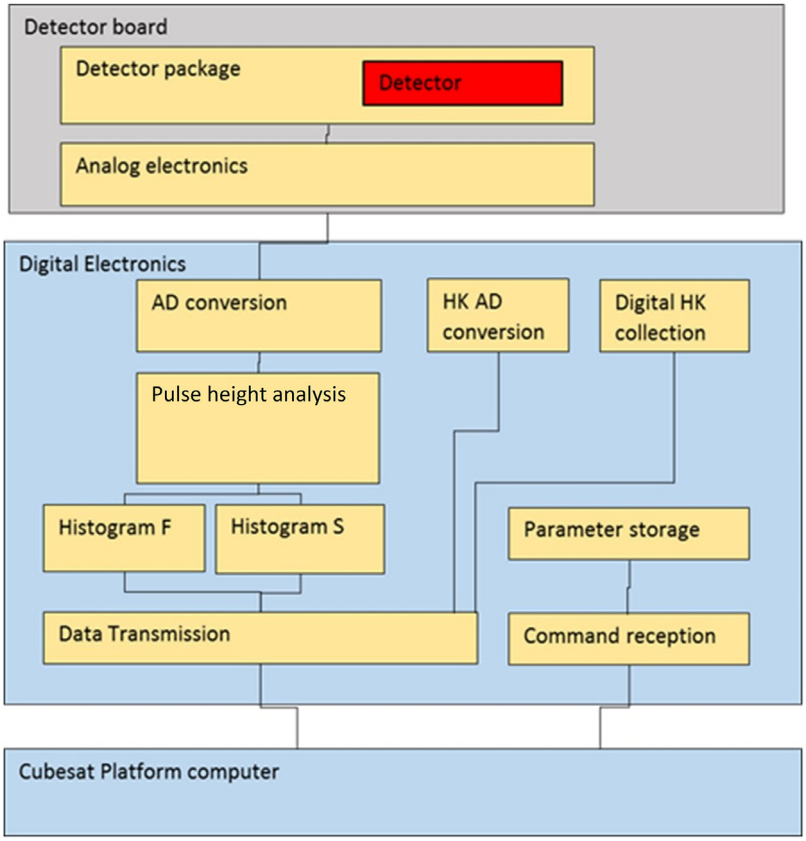

Fig. 3. High level block diagram of XFM-CS instrument.

eliminates the pulse tails, which makes the system very fast compared to the analog pulse shaping technique used in the heritage instruments.

Digital pulse processing is based on a hard-coded FPGA-logic (field programmable gate array). In addition to the basic pulse height analysis, the FPGA creates histograms (spectra) from the data. The spectral products can then be transferred to the S/C platform on commands. In addition, the FPGA collects the housekeeping (HK) data (voltages, current consumptions, temperatures, etc.) and is in general in charge of system commanding, data receiving and transmission. The data collection and system control parameters are available to the system via programmable registers. A separate power supply unit board generates the voltages needed in the electronics and the detector.

2.4. Data products

XFM instruments produce two types of science data, spectrum data and flux data. Both types of data are built with a multichannel analyzer technique familiar from nuclear physics. The detected events are sampled by their intensity value in a histogram, where each channel corresponds with an energy value. The spectrum data has 512 evenly spaced channels in energy domain. The number of channels is fixed and cannot be changed during the operations. The energy range is nominally 0–30 keV. The highest energy channel is an integral channel that counts all detected events with energies higher than 30 keV. In addition, the spectrum data packet also includes timestamps and the values of the scientific counters and number of integrator resets (dependent on leakage current) during the spectrum integration period. The baseline cadence of the spectrum data packets is 60 s, and can be changed by a telecommand.

The flux data is built with the same principle as the spectrum data. It has 6 energy channels, each of which include multiple adjacent spectrum channels and thus a wider energy range. The bounds of the flux channels can be adjusted with telecommand parameters. The number of flux channels is hard-coded (6) and there is no overlap of channels. The low and high limits of the flux channels are specified as, and correspond to the channel numbers of the Spectrum packet. The nominal flux channel ranges given in keV are presented in Table 1. The nominal channel bounds were chosen so that correspondence to GOES channels can be achieved by summing flux channels 2–4 for the GOES Long channel and channels 3–5 for the GOES Short channel. Similarly to spectrum data, flux data packet also includes timestamps and the values of the same scientific counters during the integration of the data. The baseline time resolution of the flux data is 1 s, and can be changed by a telecommand to higher values (multiples of 1 s), if there is e.g., need to limit the volume of telemetry rate without loss of time coverage.

XFM also produces HK data, which is used to monitor the health of the instrument and for the calibration of the science data products as part of the science processing pipeline (see Section 3). The HK data cadence can be changed by a telecommand.

3. Instrument characterization

Ground calibrations of XFM-CS were performed on September 21–October 6 2020 at the facilities of the Finnish Meteorological Institute (FMI), University of Helsinki (UH) and Isaware Oy. The purpose of the calibrations was to characterize and verify the science performance of the XFM-CS detector. The final data analysis is based on the experimental results obtained from the ground calibrations. The data acquisition and instrument operation was performed with electronic ground support equipment (EGSE) designed for XFM-CS. It consists of a PC with EGSE software, which connects to the S/C - XFM-CS interface simulator by USB. The instrument itself was powered by a laboratory power supply.

The characterization procedures were very similar to those used in characterization of the heritage instruments SMART-1 XSM [1],

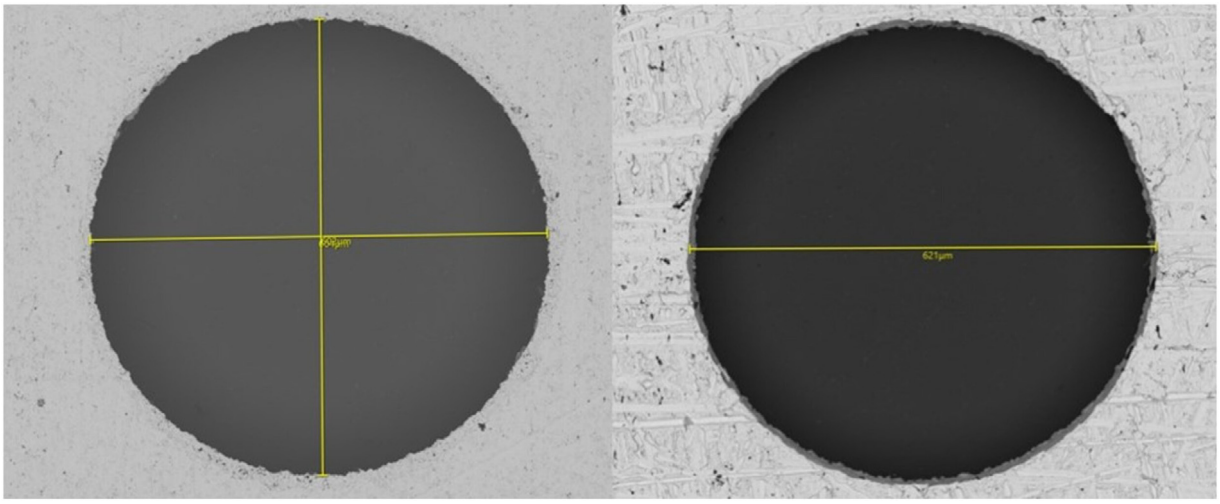

Fig. 4. Scanning electron microscope images taken of the XFM-CS detector's aperture hole from above (left) and below (right). The aperture hole is slightly conical in shape with effective diameter 0.6029 (above) and 0.621 (below).

Chandrayaan-1 XSM [4] and BepiColombo SIXS X-ray detection system [12]. The biggest difference is that unlike the heritage instruments, XFM-CS does not include an in-flight calibration source for calibration of the energy scale and energy resolution during the mission. The same is true for the present design of future XFM instruments. Instead, the energy scale and energy resolution were characterized carefully as functions of temperatures of the read-out electronics and the leakage current, respectively, before the mission. This decision was made because we have not detected any major changes in the energy scales or resolutions during the missions with heritage instruments that could not be explained by changes in temperature and/or leakage current. Also, the primary purpose of XFM instruments is operation as X-ray flux monitors, and therefore the highest possible spectrum resolution is not the primary goal, although the accuracy of the spectrum scale and the energy vs. channel conversion is vital for accurate physical fluxes.

The characterization process of XFM-CS included determination of the detector's effective area vs. photon energy and the position of the Sun in the detector's FoV, calibration of the energy scale vs. the temperatures of the detector and the (analog) read-out electronics, determination of the energy resolution as a function of photon energy and the leakage current, and the determination of the instrument's dynamic range.

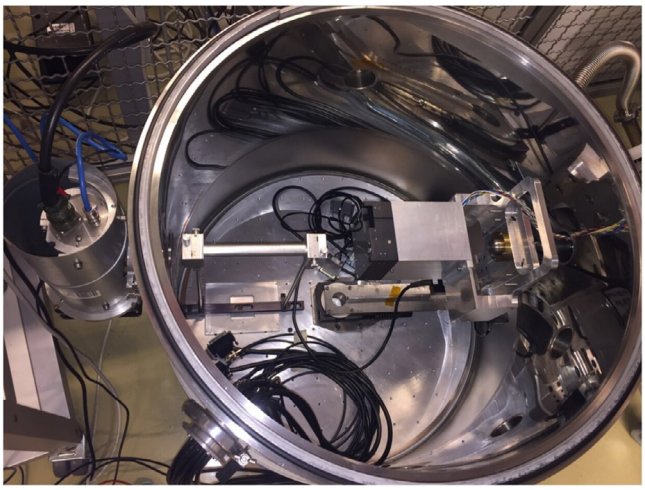

Fig. 5. XFM-CS flight model inside the vacuum chamber at the University of Helsinki. The X-ray beam collimator is seen on the left. On the chamber wall are also the openings for cables. At the center is a goniometer and an adjustable table for the device under test. The X-ray tube is seen on the left mounted on the chamber's outer side next to another opening and the collimator.

3.1. Determination of the effective area

Detector's effective area is a product of the geometric area of the exposed sensitive volume and the quantum efficiency (absorption probability within the sensitive volume) of the detector.

$$A_{eff}(E,\theta,\varphi) = G(\theta,\varphi) \cdot QE(E,\theta) \tag{2}$$

where G is the projected geometric area, QE is the quantum efficiency, E is the photon energy, θ is the off-axis angle and φ is the roll angle (azimuth) of the incident radiation. The on-axis geometric area was determined by measuring the physical area of the detector's aperture hole from images taken by the detector manufacturer before assembly with a scanning electron microscope (SEM) (Fig. 4). The SEM images with dimensional scales were used for quantifying the area of each pixel and the number of pixels in the aperture hole area, identified by their gray shade values, were counted to determine the area of the aperture hole. This process was repeated with the SEM images taken from above and below the aperture, and the results were averaged. The result is $\mathbf{2.855 \cdot 10^{-3}\ cm^2}$, which corresponds to effective aperture diameter of **0.6029 mm**.

The angular dependence of G was taken into account by measuring a static output from an X-ray tube at on-axis direction and at 10 different off-axis angles between −7° and +7° in the 4 evenly spaced orthogonal azimuthal directions (total 41 values). The measurements were performed in a vacuum chamber at the University of Helsinki, using an Oxford X-ray Technologies model XTF-5011 Ti-anode X-ray tube as the radiation source. 12 layers of Kapton tape were applied to the X-ray beam collimator in order to limit the X-ray flux well below the upper limit of the dynamic range of XFM-CS. The pressure within the chamber was stabilized at ∼4.5 mbar. The measurement setup is shown in Fig. 5. The orientation of the coordinate axis is shown in Fig. 6. The detector's boresight (on-axis direction) is along the positive Z-axis.

The results were then divided with the theoretical total QE values calculated with XDECO (X-ray Detector Configurator) version 3.0, to obtain the values of the projected geometric area in these directions, and interpolated using expected angular dependence (cosine law) to obtain G throughout the detector's FoV. XDECO is an unpublished SW tool for simulation and display of the total effective area of a generic X-ray instrument as a function of photon energy. XDECO calculates

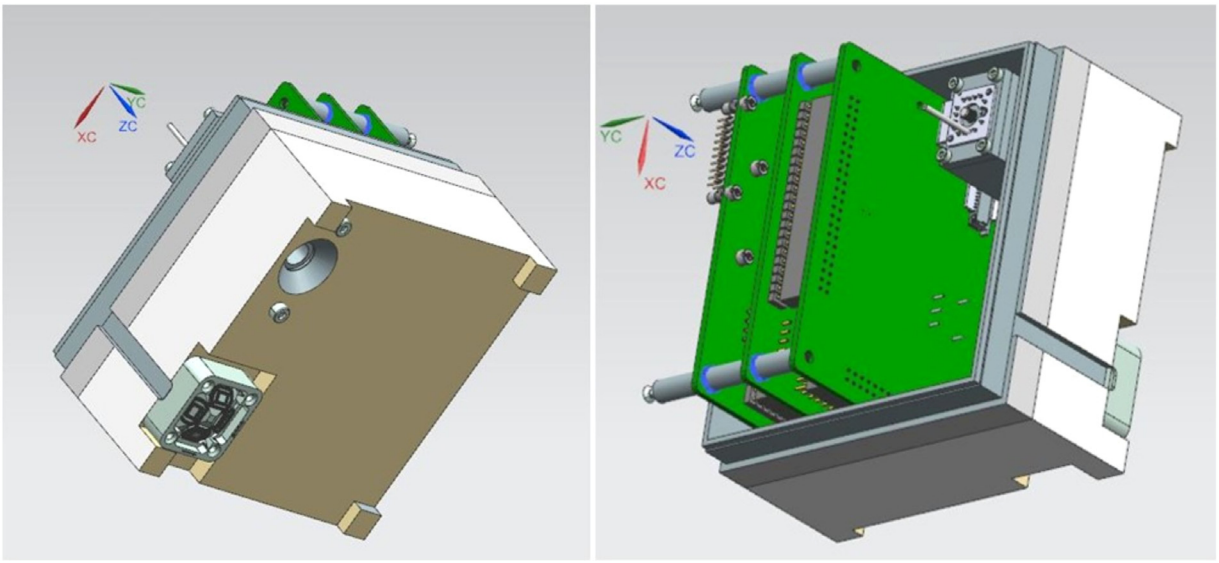

Fig. 6. CAD model of XFM-CS showing the orientation of the instrument's coordinate axis. The instrument and the SUNSTORM 1 S/C coordinate systems are identical.

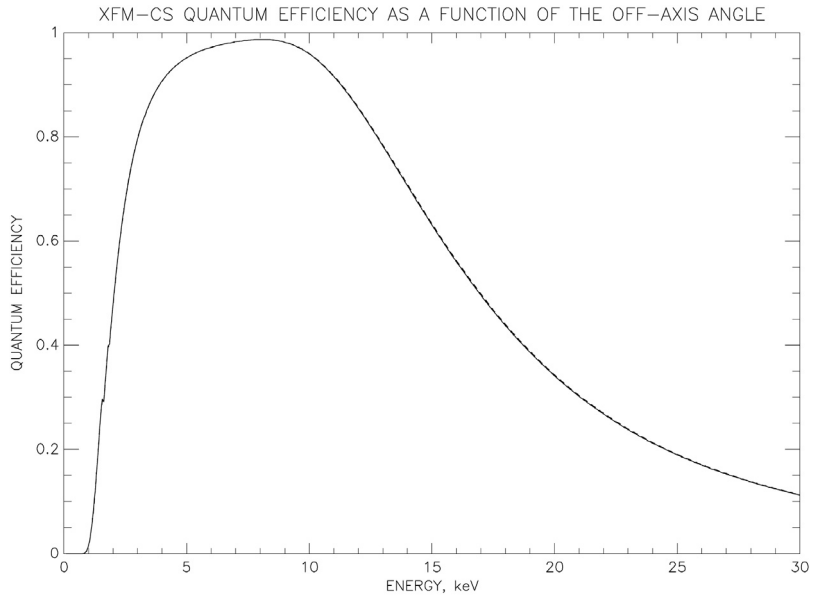

Fig. 7. XFM-CS quantum efficiency as a function of photon energy and the off-axis angle. The figures are plotted at 1° steps, but due to the narrow FoV of the instrument, the difference of QE between the center and edge of the FoV (off-axis angles 0° and 5°) is barely detectable. The figure also shows that the practical lower limit of XFM-CS's energy range is 1 keV.

the total quantum efficiency of a detector by theoretical modeling of the combined effect of filter/window transmissions, detector quantum efficiency, and the effective area of the optics, as functions of photon energy. The code is based on atomic and nuclear data tables from [13] and it has been verified by comparison of results obtained with a similar tool developed by the predecessor of XFM-CS detector manufacturer for ESA, and a Web tool provided by HEASARC (NASA). The theoretical QE curves as functions of photon energy at different off-axis angles are shown in Fig. 7 and the projected geometric area as a function of off-axis and roll angles, normalized to the on-axis response, is shown in Fig. 8.

Eq. (2) was then used to form a complete map of the detector's effective area over the entire FoV. The result is presented for roll angle $\varphi = 0°$ in Fig. 9. The A_{eff} map is a 3D table from which the detector's effective area information is interpolated according to the position of the Sun in the FoV, and used to form the ancillary response files (ARF) for spectral analysis of the XFM-CS data products.

3.2. Determination of the energy scale

The energy scales of the heritage instruments were calibrated between or during observations with an in-flight calibration source. XFM instruments, however, use a different approach. They contain no in-flight calibration sources and the energy scale calibration is done before launch. We have not detected any major changes in the energy scales during the operation of the heritage instruments with the exception of their temperature dependence. The energy scales of the Si PIN based heritage instruments were found to depend on the temperature of the read-out electronics in a nonlinear way due to the sensitivity of a field effect transistor to the ambient temperature, as described in [4,12]. The temperature of the detector chip on the other hand was found to have no effect on the energy scale [12]. However, due to the differences in the read-out electronics of XFM and the heritage instruments, XFM instruments' energy scales were found to depend on both the temperature of the analog read-out electronics and the temperature of the SDD.

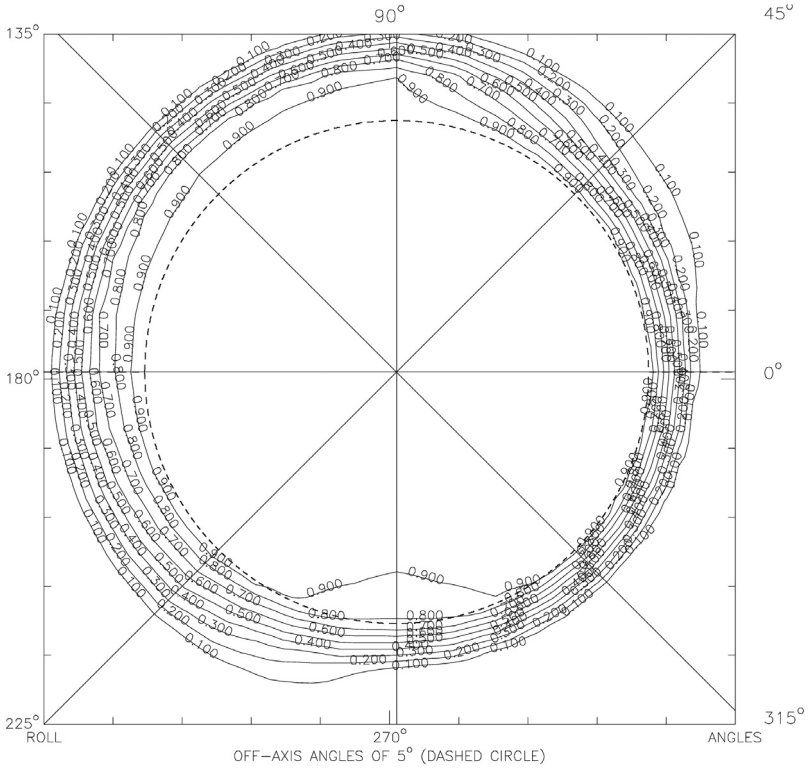

Fig. 8. Geometric FoV sensitivity of the XFM-CS FM detector. The dashed line indicates the nominal scientific FoV of 5° radius. The figure shows that the detector's FoV fulfills the requirement about the scientific FoV (Table 1).

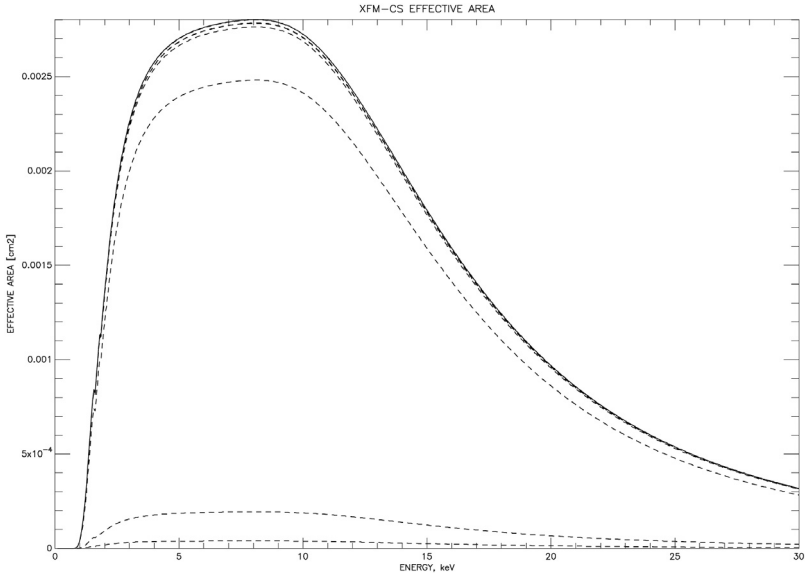

Fig. 9. Effective area of XFM-CS detector as a function of photon energy at different off-axis angles along roll angle of 0º. Solid line represents the on-axis effective area and the dashed lines are the effective areas at off-axis angles from 1° to 7° with 1° steps. It can be clearly seen that the effective area changes little within the detector's 5° scientific FoV.

Therefore the energy scales of XFM instruments must be calibrated vs. both temperatures, forming 2D look-up tables from which the energy scales are interpolated according to the temperatures.

The energy scale of XFM-CS was calibrated by observing radiation from known sources, identifying the spectral lines with known energies, determining their centroid channels, and making a linear fit as channel vs. photon energy. The measurements were performed inside a climate chamber at the facilities of FMI. An ^{55}Fe source and an ^{241}Am source were used as radiation sources, providing spectral lines at 5.90 keV (Mn K_α), 6.49 keV (Mn K_β) and 20.78 keV (Np L_γ) within the spectral range of XFM-CS. In addition, gamma radiation from the ^{241}Am source also induced fluorescence radiation from the detector's aperture, providing additional spectral lines at 9.71 keV (Au L_α) and 11.44 (Au L_β), which were also used in the analysis for improved accuracy. The measurement setup is shown in Fig. 10, and an example spectrum measured with XFM-CS is shown in Fig. 11. The peaks were fitted with Gaussian

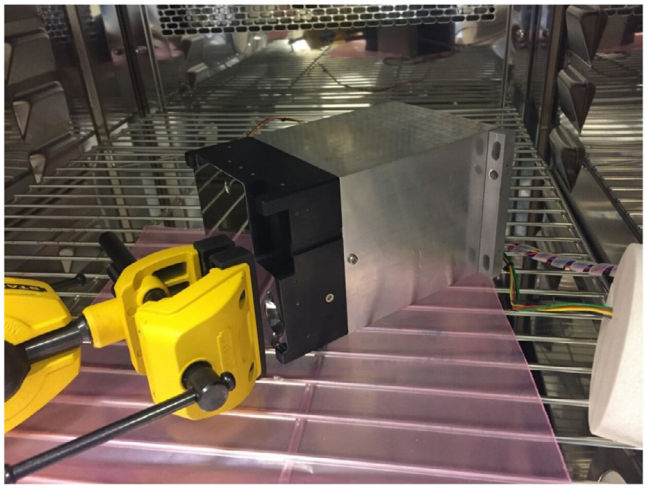

Fig. 10. XFM-CS flight model inside the climate chamber at the Finnish Meteorological Institute. The radiation sources were attached to the yellow colored adjustable holder next to the detector. XFM-CS was connected to the EGSE by cables on the right.

functions to determine their centroid channels. A linear fit was then made to the centroid channels vs. their known energies to determine the gain and offset of the energy scale.

The temperature dependence of the energy scale was determined by repeating the measurement at different operational temperatures of both the analog read-out electronics and the SDD. The measurements were made using 10 K steps in temperature throughout the instrument's operational temperature range. The climate chamber was used to stabilize the temperature of the read-out electronics and the detector's internal Peltier cooler was used to stabilize the temperature of the SDD. The resulting temperature maps of the detector's gain and offset were then interpolated to form look-up tables of the instrument's energy scale vs. temperature throughout its operational temperature range with 1 °C steps. The interpolated temperature maps of the gain and offset are shown graphically in Fig. 12.

Electronic noise count rate of XFM-CS was determined jointly with determination of the energy scale by measuring spectrum for 10 min with no stimulus present. The instrument was kept at room temperature and the temperature of the SDD was stabilized at −5 °C. The low energy threshold was set to its default value < 1 keV. The number of noise counts detected during the 10 min period was 49, which corresponds to the electronic noise background count rate of **0.063 cps** with just Earth's surface level background radiation present. This analysis shows that the low energy noise peak is below 1 keV in normal operating temperature of the XFM-CS detector. The lower limit of the energy range of XFM-CS is therefore 1 keV, which is the lowest energy at which the detector's quantum efficiency is significantly higher than zero (see Fig. 7).

3.3. Determination of the energy resolution

Similarly to the calibration of the energy scales, the calibration of energy resolutions of the heritage instruments was performed between and during observations with in-flight calibration sources. The calibration of their energy resolutions during ground calibrations, as described in [4,12], was done mainly for performance verification purposes. With XFM instruments the energy resolution is instead calibrated only before launch, forming a look-up table from which the energy resolution as a function of photon energy is interpolated.

Energy resolution of a solid state detector is known to follow the relation [14]

$$\Delta E\,(E)_{FWHM} = 2.355\sqrt{F\eta E + (\eta r)^2} \tag{3}$$

where E is the photon energy, F is the Fano factor (~0.12), η is the energy required to create an electron–hole pair in the detector material (3.6 eV in Si) and r is the total electronic (rms) noise of the detector. It can be estimated with equation [15]

$$r^2 \approx A_1 \frac{k_B T C^2}{\tau} + A_2 \left(qI + \frac{2k_B T}{R} \right) \tau + A_3 C^2 \tag{4}$$

where q is the elementary charge, T is the detector's temperature, R is the equivalent total resistance parallel to the preamplifier input, C is the preamplifier total input capacitance and τ is the pulse shaping time. Constants A_1, A_2 and A_3 are constants that depend on the pulse shaping filter used. The electronic noise consists of three components: series noise, which is inversely proportional to the square root of τ, parallel noise, which is directly proportional to the square root of τ, and the low frequency $1/f$ noise, which does not depend on τ. The leakage current dependent term of the parallel noise is the dominant type of electronic noise in a detector that has received high doses of radiation and sustained significant amounts of displacement damage. Its increase is the reason for the gradual degradation of detector performance due to radiation in space. Therefore Eq. (4) can be simplified as

$$r \approx \sqrt{A_2 q I \tau} + r_0 \tag{5}$$

where r_0 is the electronic noise from other sources than the fluctuations of the leakage current. The constant A_2 in Eqs. (4) and (5) is close to unity. Its exact value depends on the type of filter used in the shaper. Thus, the detector's energy resolution as a function of leakage current can be estimated by combining Eqs. (3) and (5) and making a fit to the data on observed energy resolutions measured with different leakage currents, keeping r_0 as a free parameter. The leakage current can be varied by operating the detector at different temperatures, as it is known to have strong nonlinear temperature dependence.

The determination of the energy resolution of XFM-CS was performed in the vacuum chamber at the University of Helsinki, jointly with the determination of the effective area (Section 3.1). The X-ray tube was used as the primary radiation source. It was attached to the outer wall of the chamber behind the instrument. Two fluorescence targets were attached to the inner collimator window to provide the characteristic spectral lines that were used for determination of the energy resolution. They were a powder mixture of Al (1.49 keV), Ca (3.69 keV) and Cu (8.05 keV), and a Pb plate (2.35 keV, 10.50 keV and 12.62 keV). The setup is shown in Fig. 13.

Energy resolution of each spectral line was determined with a Gaussian fit. The energy resolution as a function of photon energy was then determined by fitting a theoretical model (Eq. (3)) to the data. The process was repeated at different SDD temperatures for the determination of the leakage current dependence of the energy resolution. The temperature range was -40 °C to +20 °C with 10° steps. The detector's Peltier cooler was used to stabilize the SDD temperature at each step. An example fluorescence spectrum is shown in Fig. 14. The fitted energy resolution curves (Eq. (3)) at different SDD temperatures are presented in Fig. 15.

The relatively large uncertainties of the measured energy resolutions seen in Fig. 15 are partly due to the low count rate of fluorescence radiation from the fluorescence targets and partly due to the slow increase of the preamplifier temperature during the spectrum integration. Nevertheless, it can be seen from Fig. 15, the temperature dependence of the energy resolution at Beginning-Of-Life (BOL) is negligible and smaller than the accuracy of the experiment. This result was confirmed by theoretical calculations of the effects of leakage current (Eqs. (3) and (5)), which indicate that the increase of leakage current from 1.81 pA (measured at −40 °C) to 13.60 pA (measured at +20 °C) should degrade the energy resolution by only ~5 eV. The leakage current is, however, expected to increase accumulatively during the mission due to radiation damage by energetic particle bombardment in space. Therefore Eq. (5), fitted to the calibration results at BOL, excluding poor fits at −20 °C, -30 °C and -40 °C, were extrapolated to higher values of leakage current

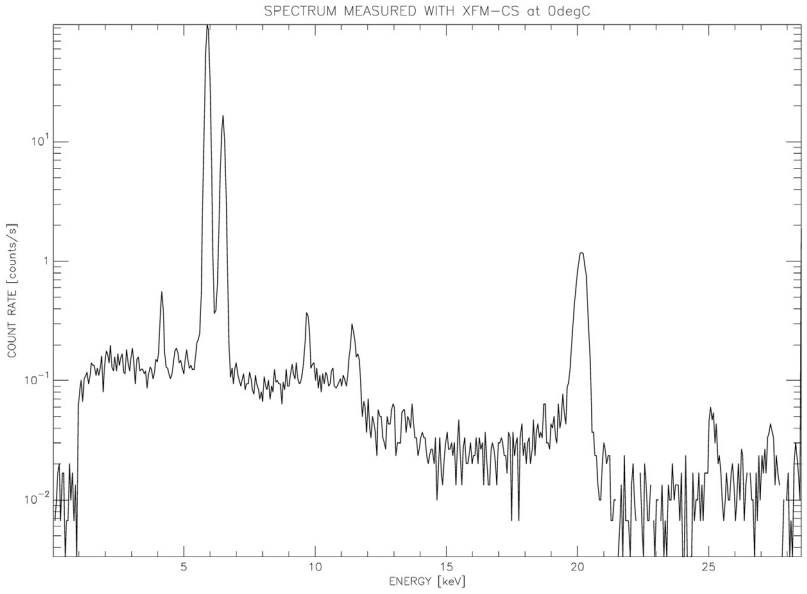

Fig. 11. A spectrum measured with XFM-CS flight model at 0 °C temperature of both the read-out electronics and the detector. The visible peaks from lowest to highest energy are: Mn K_α escape peak (4.16 keV), Mn K_α (5.9 keV), Mn K_β (6.49 keV), Au L_α (9.71 keV), Au L_β (11.44 keV), Mn K_α pile-up peak (11.8 keV), Np L_γ (20.78 keV) and ^{241}Am gamma ray line (26.4 keV). The Au lines are fluorescence from the XFM-CS detector's aperture induced by the 59.59 keV gamma radiation from the ^{241}Am source. The other lines are directly from the radiation sources. The two Mn peaks, the Np L_γ peak and the two Au L peaks were used for determination of the energy scale.

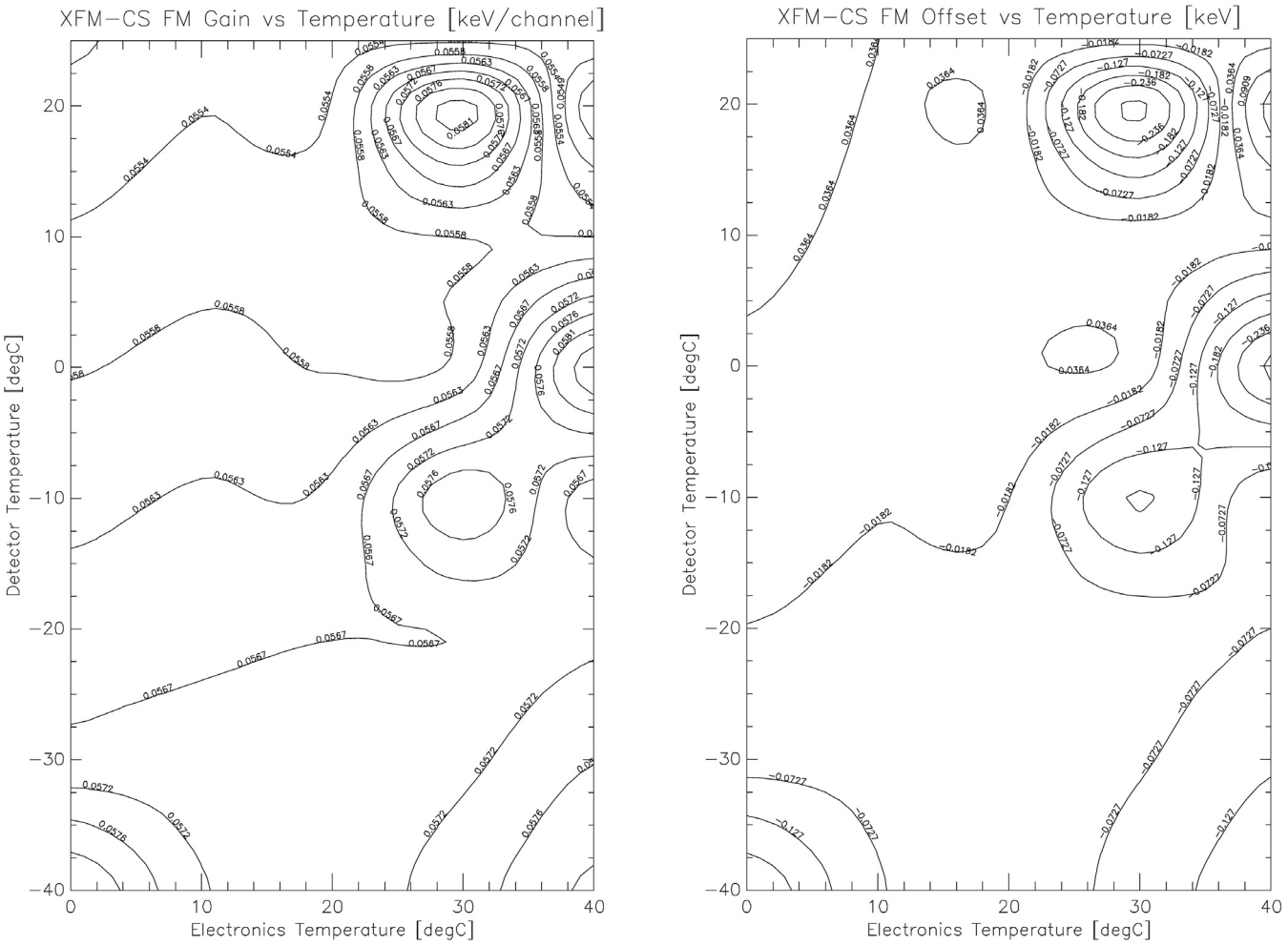

Fig. 12. Temperature maps of XFM-CS detector's gain (left) and offset (right).

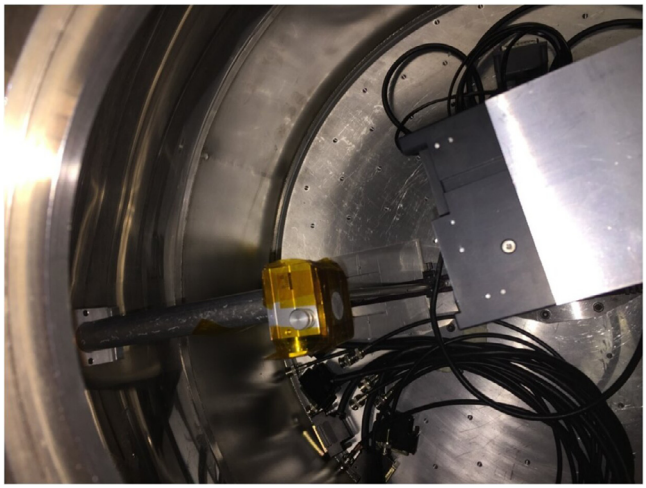

Fig. 13. Measurement setup for the determination of energy resolution. Fluorescence targets were taped on the inner slit of the X-ray tube collimator and the X-ray tube was moved to another opening in the chamber wall so that the beam illuminated the fluorescence target from behind and left of the detector. The fluorescence target shown here is the powder mixture of Al, Ca and Cu on a brass frame.

to estimate the relation between the energy resolution and the leakage current in a wider range. The result is shown in Fig. 16.

The resulting look-up table about energy resolution vs. photon energy and the leakage current will be used together with theoretical calculations about relative intensities of the different components of the Hypermet function [16] at different photon energies to form the redistribution matrix files (RMF) that are required for the spectral analysis of the XFM-CS data products. The detector manufacturer estimates the worst case total non-ionizing dose XFM-CS will sustain during the planned duration of the whole mission (2 years) to be $1.6 \cdot 10^{10}$ cm^{-2} as 1 MeV equivalent neutron fluence, taking into account the shielding effect of the detector's aluminum collimator. Assuming linear increase of leakage current due to non-ionizing dose and taking the damage factor for a well annealed Si lattice from [17], we calculate that the leakage current will increase to about $9.16 \cdot 10^{-11}$ A towards the end of mission. Thus, we see from Fig. 16 that the energy resolution is expected to be better than **200 eV at 6 keV** during the whole mission. XFM-CS therefore clearly fulfills the requirement of < 400 eV end-of-life (EOL) energy resolution at 6 keV (Table 1). It should be noted that this approach does not take into account the possible changes in electronic noise due to any sources independent of leakage current. For example, the detector manufacturer has detected a slight increase in electronic noise due to total ionizing dose effects on the detector's anode and charge sensitive amplifier (CSA) during radiation testing of SDD detectors. The effects of this noise are insignificant to X-ray fluxes and also very minor in the spectra. However, an in-flight X-ray calibration source would be the most reliable way of determining the energy scale and energy resolution of X-ray spectra onboard space missions, and would guarantee the highest possible accuracy of scientific analysis, e.g., in the determination of the ionization state of the highly ionized Fe lines around 6.5 keV.

3.4. Determination of the dynamic range

Lower limit of a detector's dynamic range is determined by the lowest S/N, with which a sufficiently accurate spectral analysis is possible. In Section 2.1 we noted that by our experience we estimate that reliable spectral analysis is possible with a minimum number of spectral counts N ~200. In order to determine the lower limit of the dynamic range of XFM-CS, we used the detector's on-axis sensitive area (Section 3.1) to calculate the minimum photon flux during a 60 s spectrum integration time, which produces a spectrum with $N > 200$. The result is 1200 photons/cm^2/s. Assuming typical solar X-ray spectrum during quiescence (bremsstrahlung continuum with $T \approx 2.7 \cdot 10^6$ K) and taking into account the detector's on-axis quantum efficiency (Fig. 7), this corresponds to about $\mathbf{4 \cdot 10^{-9}\ W/m^2}$ above 1.55 keV (GOES flux A0.4). This is significantly below the scientific requirement for the lower limit, which is $2 \cdot 10^{-7}$ W/m^2. Thus, the dynamic range of XFM-CS extends much further into the low intensity range than was required. It covers the whole solar X-ray intensity scale at the lower end and thus XFM-CS is able to provide useful data even during the time periods when the Sun is at its most quiescent state.

The upper limit of the detector's dynamic range is limited by pile-up. If the time interval between detected events is too short, multiple events are summed up and are counted as single event. Determination of the dynamic range therefore requires characterization of pile-up at high count rates. Due to the very high count rate requirement, the determination of the XFM-CS dynamic range was performed in a vacuum chamber at the University of Helsinki (Fig. 5), jointly with determination of the effective area. The measurement setup was identical to that shown in Fig. 5 except for the Kapton filters, which were removed from the X-ray beam collimator. The pile-up counts at 19 different total count rates were counted and a Poisson statistical function (Eq. (1)) was fitted to the results. The speed of the XFM-CS read-out electronics and the whole system was determined from the data for comparison with measurements of the electronics speed by the manufacturer, and theoretical estimates of the amount of pile-up at different count rates.

Pile-up occurs if the time interval between two successive photons is shorter than the pulse pair resolution time τ_p (Eq. (1)). It results in two or more events being counted as a single event whose energy is the sum of their energies, causing distortion of the spectrum towards higher energies. The apparent hardening of the solar X-ray spectrum may result in overestimation of the plasma temperature distribution, which can lead to false conclusions about the physical properties and dynamics of the coronal plasma (density, elemental abundances, FIP bias, etc.). This deformation of the spectrum becomes gradually more significant as the count rate and the amount of pile-up increases. It cannot be corrected with any realistic solution, and it affects the calibrated flux data as well because the spectrum shape is taken into account in converting the raw flux data into physical units (see sect. 3.5). Based on our experience with XSM instruments, we have estimated that the highest amount of pile-up in a spectrum with only sufficiently minor deformations for reliable spectral analysis is ~6%. The practical upper limit of the dynamic range is therefore the highest photon flux, where < 6% of the events are piled-up. The probability of pile-up occurring can be calculated for any total count rate I using Eq. (1). Keeping the X-ray tube high voltage at 8.5 kV, thus limiting the photon energy in the beam to 8.5 keV, it is possible to estimate the amount of double ($n = 1$) and triple pile-up ($n = 2$) in the spectrum. The contribution of higher than 2nd order pile-up ($n > 2$) is statistically negligible. The amount of pile-up was determined for 19 evenly distributed count rates between 0 and 400 kcps, and Eq. (1) was fitted to the results (Fig. 17), keeping the pulse pair resolution τ_p as a free parameter. The result is $\tau_p = \mathbf{202.2 \pm 2.0\ ns}$. Knowing the pulse pair resolution time allows estimation of the amount of pile-up at different count rates using Eq. (1). The practical upper limit of the dynamic range is the count rate I, with which the pile-up probability $P_{pile-up} = 6\%$. For XFM-CS flight model $\boldsymbol{I_{6\%} \approx 306\ kcps}$. Assuming typical solar X-ray spectrum during high flux conditions and taking into account the detector's on-axis quantum efficiency (Fig. 7), this corresponds to physical flux $9.2 \cdot 10^{-4}$ W/m^2 (GOES flux X9.2). This is slightly below, but very close to the designed upper limit of the dynamic range (X10), giving confidence to our method for determining the goal design values for the future versions of XFM for operative missions. The limit set for the maximum allowed pile-up is also not a hard limit, and the pile-up increases only gradually even well above the limit. There are also no other effects than

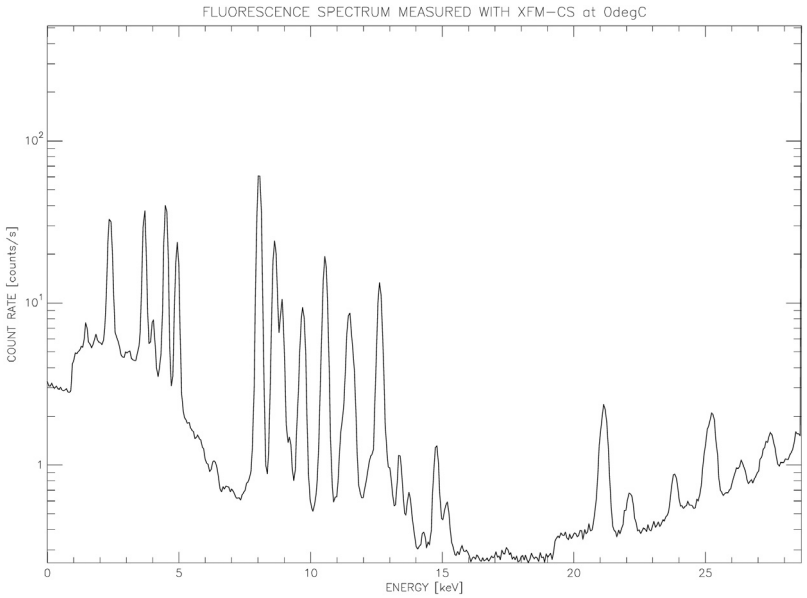

Fig. 14. A fluorescence spectrum measured at detector temperature 0 °C. The visible peaks from lowest to highest energy are Al K_α (1.49 keV), Pb M_α (2.33 keV), Ca K_α (3.69 keV), Ca K_β (4.01 keV), Ti K_α (4.51 keV), Ti K_β (4.91), Cu K_α (8.05 keV), Zn K_α (8.64 keV), Cu K_β (8.91 keV), Zn K_β (9.57 keV) blended with Au L_α (9.71 keV), Pb L_α (10.55 keV), Au L_β (11.44 keV). Pb L_β (12.61 keV), Au L_γ (13.38), Pb L_γ (14.76). Ti peaks are scattered photons from the X-ray tube that was used as the primary radiation source. Zn lines are from the fluorescence target's brass frame and Au lines are fluorescence from the detector's aperture. They are induced by high energy X-rays that can penetrate the instrument's aluminum casing and the detector's steel cup, as can be seen from the continuum above 20 keV. The peaks above 20 keV might be due to Bragg scattering of the X-ray beam from the fluorescence targets. All other lines are from the fluorescence radiation from the targets. Eight highest peaks were fitted with Gaussian functions for the characterization of energy resolution.

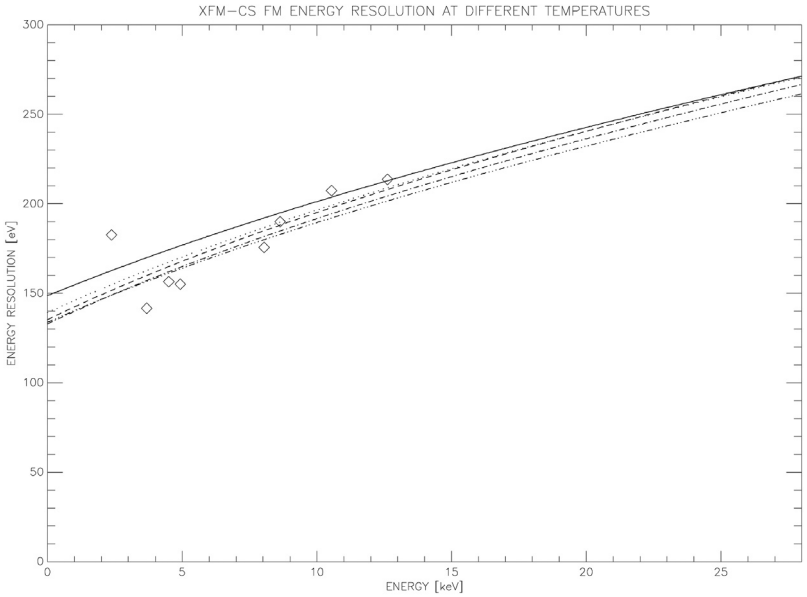

Fig. 15. Energy resolution of XFM-CS at different detector temperatures from -20 °C to +20 °C at 10 degrees steps. The lines correspond to energy resolutions at -20 °C (solid line), -10 °C (dashes and triple dots), 0 °C (dashes and dots), +10 °C (dashes) and +20 °C (dots). The symbols are the measured energy resolutions of the fluorescence lines at 0 °C. The differences of the energy resolution at different temperatures are smaller than the accuracy of the experiment. Resolutions measured at detector temperatures -40 °C and 30 °C are not included in the figure because the detector gain had shifted slightly during the 1h spectrum integration due to increasing temperature of the read-out electronics, which resulted in poor quality fits to the fluorescence lines. The heating effect was primarily caused by the operation of the detector's Peltier cooler at high power (large ΔT), and it is also visible to a lesser degree in the resolution measured at -20 °C.

pile-up, which would saturate the detector, but only gradual increase of the deformation of the spectrum (energy distribution of events). Thus, we are very confident that using two detectors with the planned two different effective areas in the XFM for future missions, it is possible to cover, and even exceed the required flare intensity range from A2 to X20, with enough margin for significant overlap of the dynamic ranges of the two detectors, and ability to measure even extremely large X-ray flares on the Sun above the required upper limit. In the other end of the dynamic range, the more sensitive detector in future XFM instruments is more sensitive than the XFM-CS detector and achieves better S/N in quiescent conditions. Combined with the very low background, this can lead to new findings concerning micro- and nanoflares and their debated role in heating of the solar corona [18,19], as well as in understanding the FIP bias of the coronal plasma [6,20–22].

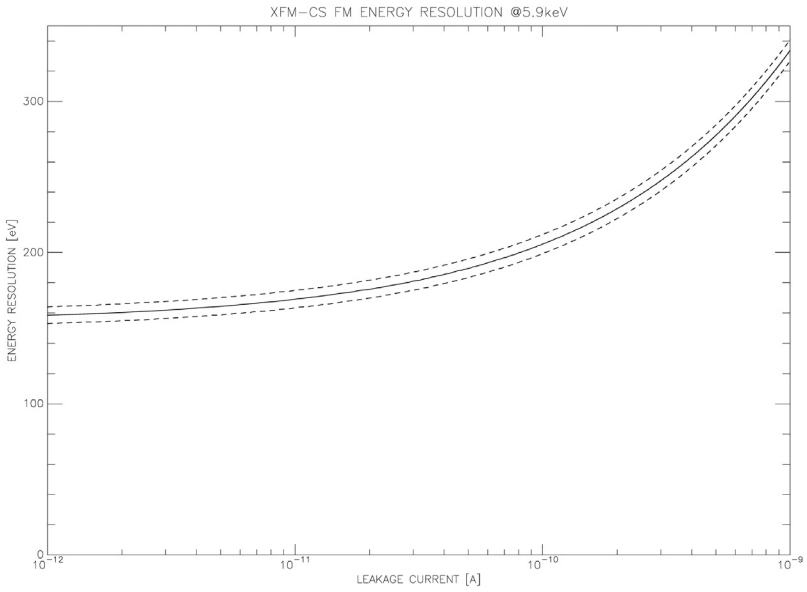

Fig. 16. Energy resolution of XFM-CS as a function of leakage current. The figure has been extrapolated by theoretical calculations (Eqs. (3) and (5)) to higher leakage currents than those observed during the calibrations (13.6 pA).

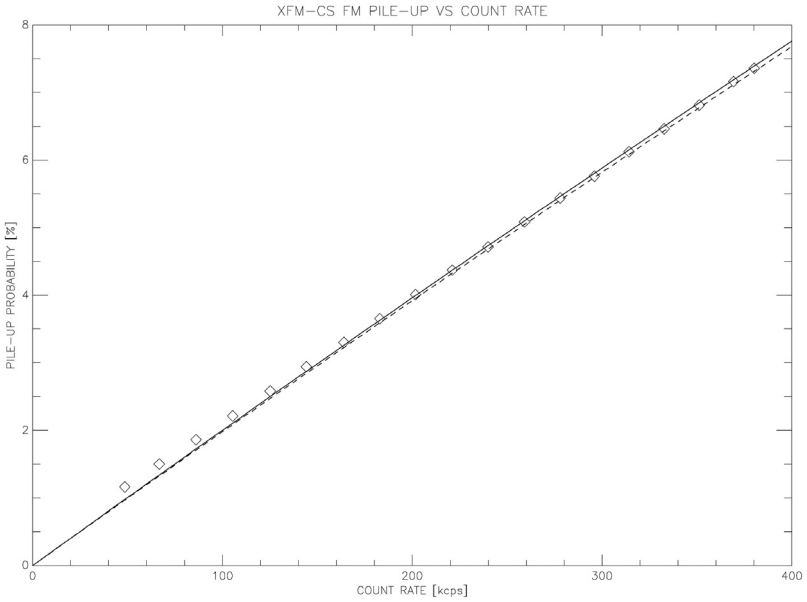

Fig. 17. Pile-up probability as a function of total count rate. Symbols are measurement results and the solid line is Eq. (1) fitted to the results. Dashed line indicates theoretical pile-up probability with $\tau_p = 200$ ns.

3.5. Summary and the science data processing pipeline

A summary of the ground calibration results and the values of the key parameters affecting the performance of the instrument are compiled in Table 3.

The ground calibration data products: A_{eff} map, temperature maps of the gain and offset and the energy resolution table form a database that is used to convert the raw science data into physical units. Data flow diagram of the science data processing pipeline is presented in Fig. 18. The pipeline script is available as both Python and IDL versions.

HK data and S/C attitude data are used to interpolate the necessary information from the calibration data tables. The effective area is interpolated by the position of the Sun in the detector's FoV (S/C attitude), Energy scale is interpolated according to the temperatures of the analog read-out electronics and the SDD, and the energy resolution is interpolated according to the leakage current.

The spectrum shape is taken into account in converting the flux data into physical units. The effective energy and sensitivity of each flux channel is determined by taking an average of all spectrum channel energies vs. their effective areas within the flux channel energy range, weighted by the number of raw spectrum counts. The spectrum data is converted to FITS format with separate calibration information (RMF and ARF) for each spectrum (default measurement cadence 60 s). RMF characterizes the spectral response of the detector. It includes the calibrated energy scale of the spectral data as well as the redistribution function, which represents the probability of a photon of a given energy being read into a certain energy channel. It is constructed from the calibrated energy scale information as well as the energy resolution information together with the theoretical calculations of the relative intensities of the different Hypermet function components [16]. ARF describes the effective area of the detector as a function of photon energy. It is constructed directly from the effective area information.

Table 3
Calibrated values of parameters affecting the scientific performance of XFM-CS.

Parameter	Requirement or nominal value	Calibrated value
Aperture diameter	0.6 ± 0.1 mm	0.6029 mm
Aperture area	$2.827 \cdot 10^{-3}$ cm^2	$2.855 \cdot 10^{-3}$ cm^2
Scientific field-of-view	5° half cone	~5° cut-off
Energy range	1 - 30 keV	1 - 30 keV
Electronic noise background	< 1 cps	0.063 cps
Energy resolution (BOL)	< 300 eV @ 6 keV < 500 eV @ 10 keV	171 eV @ 6 keV 193 eV @ 10 keV
Energy resolution (EOL, predicted)	< 400 eV @ 6 keV < 650 eV @ 10 keV	< 200 eV @ 6 keV < 250 eV @ 10 keV
Pulse pair resolution	200 ns	202.2 ± 2.0 ns
Maximum count rate (pile-up < 6%)	330 kcps	306 kcps
Dynamic range	$2 \cdot 10^{-7}$ - $1 \cdot 10^{-3}$ W/m^2 (B2 - X10)	$4 \cdot 10^{-9}$ - $9.2 \cdot 10^{-4}$ W/m^2 (A0.4 - X9.2)

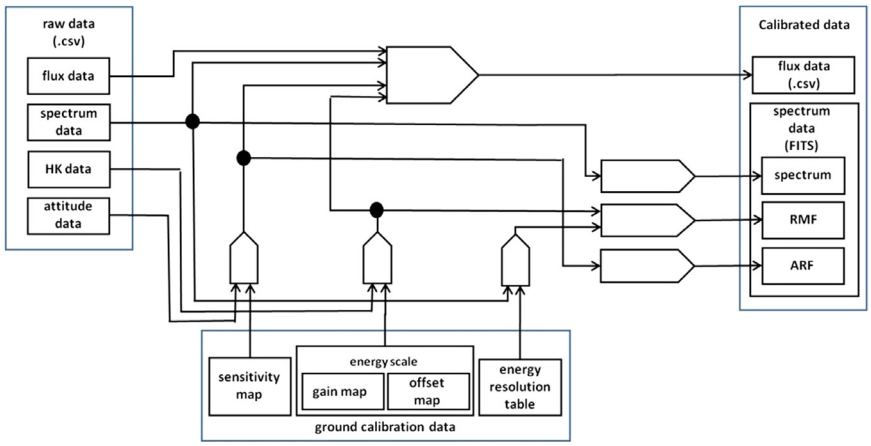

Fig. 18. Data flow diagram of the XFM-CS data processing pipeline. Relevant information is retrieved from the ground calibration data tables to convert raw science data into physical units. The calibrated flux data is in .csv format. Spectrum data with relevant calibration information is converted to FITS format, which is compatible with most common spectral analysis software packages, including XSPEC [23].

It was found during the commissioning of SUNSTORM 1 that correction for the electron background is required. It has been known since the early operation of the instruments that XFM-CS has heritage on that the solid state detectors are sensitive to high energy particles in space, electrons in particular [24]. Even a minor particle background can cause significant error to the flux measurements of solar X-rays, especially in high energy flux channels. To avoid electron contamination of the data, electron background within the spectral and flux channel energy ranges is estimated based on the amount of counts in the highest energy channel, which is an integral channel counting all events whose energy is above the spectral energy range of XFM-CS. These events are mainly caused by electrons. The estimated electron background is then subtracted from both the spectrum and flux data. More details about the electron background correction is found in Section 4.4 The correction is applied to raw data before further processing steps. In addition, a data quality flag was added to the calibrated data files as a warning for electron contamination of flux data where electron background is high enough to cause significant errors to flux measurements due to its statistical fluctuations.

4. Commissioning and first results

SUNSTORM 1 was launched to Sun-synchronous LEO with an altitude of 551 km on August 17 2021. Bi-directional communications with the satellite were established during its first pass over the ground station in Espoo, Finland. The first health checks showed both the CubeSat platform and XFM-CS being in excellent health. This was followed with the deployment of the solar panels, acquisition of Sun pointing attitude and commissioning of both the S/C and XFM-CS. The first solar X-ray spectrum was acquired on August 27 2021, i.e. just ten days after the launch. Both raw spectrum data and calibrated spectrum from this four minute first light observation are shown in Fig. 19. The spectrum was fitted with physical model (Variable) Astrophysical Plasma Emission Code (VAPEC) v3.0.9 [25], which assumes an optically-thin thermal plasma and allows modeling with variable elemental abundances. It approximates coronal plasma in quiescent conditions reasonably well even though the assumption of thermal balance is generally not valid. When modeling coronal plasma in more active conditions we extend our model to non-thermal domain by addition of a non-thermal broken power law component with Gaussian emission lines to the thermal VAPEC model.

The commissioning of SUNSTORM 1 and XFM-CS culminated in successful In-Orbit Commissioning Review on October 18 2021. Since then, XFM-CS has been conducting observations of solar X-rays with no observed deviations in the specified functionalities or performance degradation in the instrument.

A sample of the first results obtained with XFM-CS is presented in this section with the emphasis on scientific performance of the instrument and quality of the data. Three time periods of different levels of solar activity were selected for the analysis. (1) A long duration M1 flare observed on November 2 2021 was used to evaluate the instrument's performance during high solar activity. (2) A period of active conditions on November 5 2021, with occasional C class solar flares (X-ray flux > $1 \cdot 10^{-6}$ W/m^2) was used for evaluating the instrument's performance in rapidly varying X-ray flux conditions during

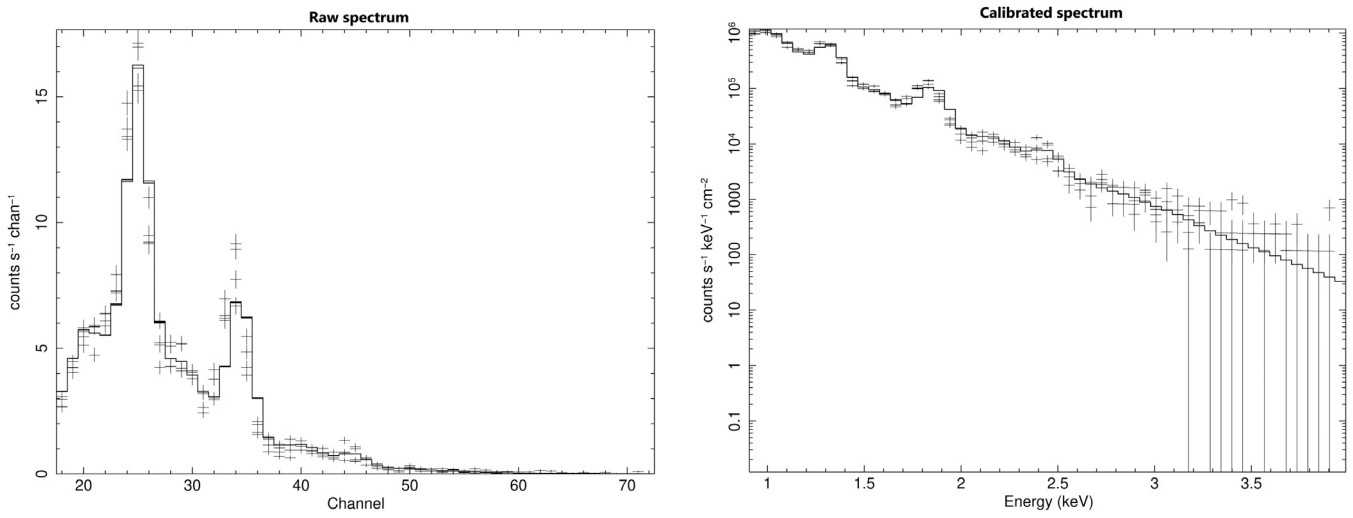

Fig. 19. Spectrum of the first light observation of SUNSTORM 1/XFM-CS (August 27 2021). Raw spectrum is shown on the left and the calibrated spectrum on the right. Fitted model is Variable Astrophysical Plasma Emission Code (VAPEC) v3.0.9 [25]. The modeled solar X-ray output was $1.2 \cdot 10^{-7}$ W/m^2 (B1.2) within the energy range of the GOES Long channel (1–8 Å, 1.55–12.4 keV).

intermediate level of solar activity. (3) Finally, quiescent period on November 20 2021 with GOES flux varying between $2 \cdot 10^{-8}$–$4 \cdot 10^{-8}$ W/m^2 (levels A2–A4) was used for evaluating the performance of the instrument near the lower limit of its dynamic range. The performance of XFM-CS has been observed to be stable in comparison with GOES X-ray sensor data also outside these time periods. As of this writing we have yet to observe any X-class solar flares with XFM-CS. The instrument was unfortunately switched off on October 28 2021 when an X1 class flare occurred.

4.1. Flux data

The calibrated solar X-ray flux data collected of the three selected time periods is presented in Fig. 20. Each panel shows 8 h of data and solar X-ray flux from six energy bands. The periodic ∼38 min gaps seen in the data are due to eclipse periods when SUNSTORM 1 is in Earth's shadow and thus XFM-CS does not have the Sun in the FoV. The shorter few minute gaps in the data are due to the Sun occasionally drifting outside the instrument's FoV. During the early operations the attitude determination and control system (ADCS) of SUNSTORM 1 used to repeatedly revert from more accurate fine pointing mode into coarse pointing mode after roughly 1 day of operations. The coarse pointing mode is only intended as a backup and its pointing stability is insufficient for constantly maintaining the pointing accuracy better than 5°. This issue has since then been resolved with a parameter update for the ADCS, and occurrences of gaps in the data due to poor pointing accuracy are rare. The longer gap in the data seen at 3:25–4:30 on November 2 2021 (Fig. 20 top) is due to an update of the mission timeline during one of the ground station passes.

The data clearly shows that the flux levels in the solar spectrum decrease towards higher energies, with larger difference at quiescent time periods. This is as expected since the soft X-ray continuum is based on thermal bremsstrahlung. At the peak of the M1 flare on November 2 2021 (Fig. 20 top), the spectrum just reaches the flux channel 5 (12.4–24.8 keV), while during the B and C class activity on November 5 2021 (Fig. 20 middle) the highest energy photons are seen in flux channel 4 (6.2–12.4 keV). During quiescent periods the spectrum barely extends above the lower limit of flux channel 3 (3.1–6.2 keV).

The data for all three time periods also has some noise in the high energy flux channels. This is caused by statistical fluctuations of the high energy electron background seen by the instrument (Section 4.4). All three time periods shown in Fig. 20 indicate that the electron contamination is at its highest a few minutes after and before the eclipse part of the orbit. At these times SUNSTORM 1 is roughly over latitudes 60°–70°, north and south respectively, where the S/C slightly touches the inner edge of Earth's outer radiation belt, which is the main source of the electron contamination.

Finally, the lowest energy channel (1.0–1.55 keV) shows cyclic behavior, where the flux increases periodically during the continuous observations, and begins again at slightly lower level after the eclipse periods. This behavior is most clearly seen in quiescent conditions (Fig. 20 bottom). This is obviously an instrument effect since the time period is the same as the orbital period of the S/C. The source of this effect is currently interpreted to be a combination of the temperature shifting of the XFM-CS energy scale and the minor uncertainties in the thicknesses of the detector materials and filters. The flux channel bounds remain fixed during individual observations, and are thus affected by the shifting of the instrument's energy scale due to thermal effects. This, combined with the very low *QE* near 1.0 keV (Fig. 7), makes the calibration of the flux at the lowest energies very sensitive to the minor uncertainties of the filter thicknesses that directly affect the *QE*. It could be possible to mitigate this effect by recalculating the *QE* iteratively by adjusting the assumed filter thicknesses until the oscillation effect of the calibrated low energy flux is minimized. Another option would be to increase the lower bound of the flux channel 1 to slightly higher energy where the *QE* is higher and less sensitive to the small uncertainties in the filter thicknesses.

4.2. Spectrum data

A sample high resolution spectrum from each of the three selected time periods is presented in Fig. 21. The spectrum from the M1 flare on November 2 2021 was measured at 03:02 UTC near the peak of the flare, the spectrum of the medium solar activity on November 5 2021 is from the beginning of the decay phase of a B8 class flare at 16:35 UTC, and the spectrum from the quiescent period on November 20th was measured at 05:40 UTC. The three spectra were fitted with a two component model, which uses VAPEC v.3.0.9 for the thermal component and broken power law with two Gaussian spectral lines (ionized Fe and Ni) for the non-thermal component. However, as expected, the emission measure of the non-thermal component of quiescent plasma was near zero. Model parameters for the three spectra are shown in Table 4.

Fig. 21 shows that the calibration of XFM-CS was successful. The spectrum shape as well as the positions and FWHMs of the emission lines of the fitted model spectra match the observed spectra well,

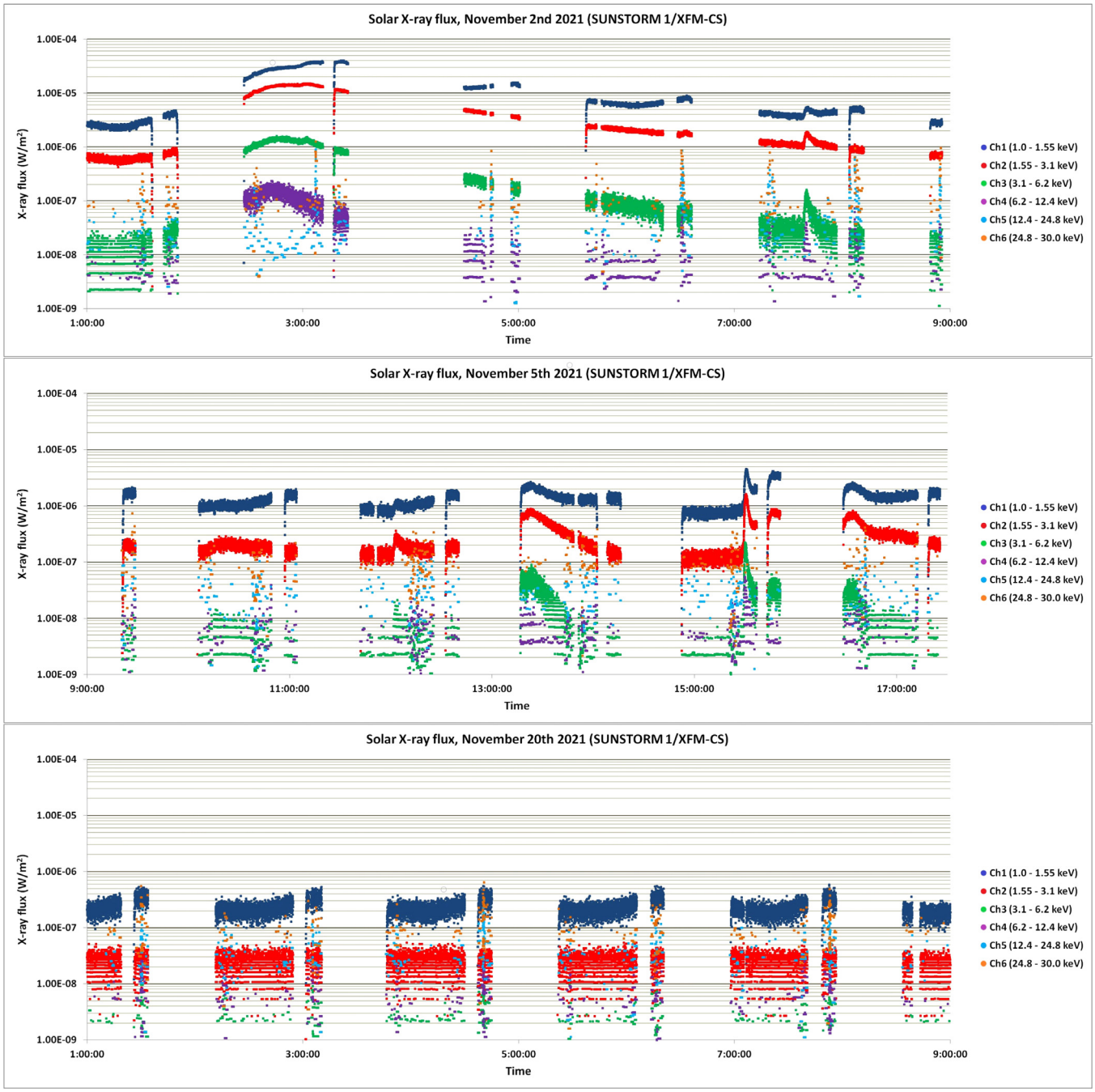

Fig. 20. Calibrated solar X-ray flux data measured with XFM-CS in period of high solar activity on November 2 (top), intermediate level of activity on November 5 (middle) and quiescent conditions on November 20 (bottom) 2021. Each panel shows eight hours of data.

which shows that the effective area, energy scale and energy resolution information retrieved from the ground calibration datafiles is accurate. The small discrepancy of the lowest energy part (~1 keV) of the *QE* curve (Fig. 7), which is explained in Section 4.1, might have a minor negative effect on the spectral fitting near the lower end of the energy range (~1 keV). The results in Fig. 21 and Table 4 also prove that the data provided by XFM-CS is suitable for spectroscopic studies of solar corona, such as investigation of the evolution of spectral parameters during flares or studies of the FIP bias of elemental abundances in the solar corona.

The emission lines of the solar X-ray spectra measured with XFM-CS are often seen to broaden towards the lower energies. Typically, this phenomenon becomes visible during the decay phase of solar flares, and it is sometimes also seen during quiescent conditions. This effect is visible in the low energy emission lines (< 3 keV) of the M1 flare on November 2 2021 (Fig. 21 left) and also in the emission lines of the first light spectrum (Fig. 19). We believe that the most likely explanation for this broadening is "evaporation" of cooler chromospheric plasma into the magnetic loops of the solar corona [26–28], which occurs especially after the impulsive energy release of a flare. This cooler plasma is at lower ionization state than the hot coronal plasma and thus emits characteristic line emission at slightly lower energies when it encounters much hotter coronal plasma, which explains the apparent broadening of the emission lines towards the lower energies.

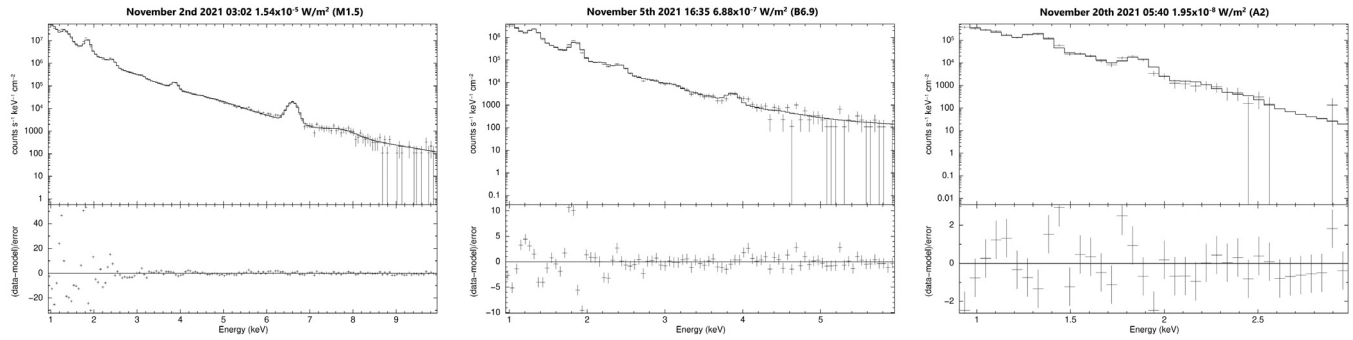

Fig. 21. Solar X-ray spectra of the M1 flare on November 2 2021 at 03:02 (left), intermediate activity on November 5 2021 at 16:35 (middle) and quiescent period on November 20 2021 at 05:40 (right). The spectra were fitted with a two-component model VAPEC 3.0.9 + broken power law and Gaussian emission lines. Included are also fit residuals divided by statistical uncertainties.

Table 4
Model parameters for the three solar X-ray spectra shown in figure 21. The element abundances are given relative to the solar photospheric abundances. Norm of the thermal VAPEC component is emission measure scaled to the distance from the source. The norms of the non-thermal components are given in photons/cm^2/s.

Parameter	02.11.2021 03:02:00	05.11.2021 16:35:00	20.11.2021 05:40:00
Temperature	0.6779 ± 0.0013 keV ~7.9·10^6 K	0.4899 ± 0.0038 keV ~5.7·10^6 K	0.2162 ± 0.0145 keV ~2.5·10^6 K
Mg	3.19 ± 0.07	2.48 ± 0.21	3.43 ± 0.64
Al	3.70 ± 0.14	1.45 ± 0.45	0.07 ± 2.47
Si	1.71 ± 0.03	1.94 ± 0.13	3.20 ± 0.93
S	0.54 ± 0.02	0.78 ± 0.09	1
Ar	0.55 ± 0.02	1.16 ± 0.39	1
Ca	5.20 ± 0.18	18.74 ± 3.90	1
Fe	0.97 ± 0.03[a]	0.73 ± 0.10[a]	0.62 ± 0.54
Ni	0.03 ± 0.25[a]	4.01 ± 1.1[a]	1
Norm (VAPEC)	5.21·10^7±1.2·10^5	4.93·10^6±6.5·10^4	3.57·10^6±1.3·10^6
Power law Index 1	1.53 ± 0.19	2.31 ± 0.93	N/A
Break Energy	4.94 ± 0.07 keV	N/A	N/A
Power law Index 2	6.75 ± 0.30	N/A	N/A
Norm (broken power law)	1.54·10^5±4.4·10^4	8260 ± 12200	N/A
Line Energy (Fe)	6.594 ± 0.006 keV	N/A	N/A
Line Sigma (Fe)	0.077 ± 0.007 keV	N/A	N/A
Norm (Fe)	4560 ± 210	N/A	N/A
Line Energy (Ni)	7.681 ± 0.105 keV	N/A	N/A
Line Sigma (Ni)	0.294 ± 0.117 keV	N/A	N/A
Norm (Ni)	360 ± 150	N/A	N/A
Model Flux (1.55–12.4 keV)	4.81·10^6 photons/cm^2/s 1.54·10^{-5} W/m^2 (M1.5)	2.23·10^5 photons/cm^2/s 6.88·10^{-7} W/m^2 (B6.9)	6880 photons/cm^2/s 1.95·10^{-8} W/m^2 (A2)

[a]The element abundances derived from the VAPEC model are not reliable for ions with K-shell emission lines > 5 keV, where the non-thermal component of the spectrum dominates.

4.3. Comparison with GOES X-ray sensor data

As noted in Section 2.4, the default energy bounds of the flux channels of XFM-CS were chosen so that channels 2–4 correspond to GOES Long channel (1–8 Å, 1.55–12.4 keV), and channels 3–5 correspond to GOES Short channel (0.5–4 Å, 3.1–24.8 keV). The comparison between the calibrated flux data from XFM-CS and primary GOES (GOES-16) X-ray sensor (XRS) for the three selected time periods is shown in Fig. 22.

Fig. 22 shows that the observed fluxes from XFM-CS and GOES match quite well. In general, solar X-ray flux measured with XFM-CS in the energy range of GOES Long channel is about 5%–10% lower than GOES XRS flux, while the fluxes are nearly identical in the energy range of GOES Short channel during the periods of solar activity when there is significant flux at higher energies.

For clarity, a more detailed comparison between the calibrated solar X-ray flux data from XFM-CS and GOES XRS data was performed by examining a 40-minute part of the observations during each of the three selected time periods. Fig. 23 includes a comparison of the XFM-CS data with simultaneous data from both primary (GOES-16) and secondary (GOES-17) GOES XRS. The XFM-CS datasets also include 60 s moving averages of the individual 1 s flux data samples for easier comparison with GOES data.

The relative difference between the lower energy X-ray fluxes (corresponding to the GOES Long channel) becomes smaller when the total flux is high. The X-ray fluxes measured with the two instruments in the energy range of GOES Short channel are nearly identical during the periods of high solar activity, while in quiescent conditions, GOES Short flux is usually higher than XFM-CS flux in the same energy band. Most of the differences are probably due to the different way the energy bounds of the flux channels are defined in the two instruments. The energy ranges of the GOES X-ray sensors are defined only by the filter transmittances of the sensors, and thus they have reduced sensitivity below their nominal channel energies [8]. This is not the case in XFM-CS, where the events are distributed to spectrum and flux channels in digital domain based on pulse height analysis. The non-zero response of GOES energy channels below their nominal energy bounds could explain not only the slightly higher fluxes measured with GOES in comparison with XFM-CS, but also the apparent decreasing of the relative difference in high flux conditions when the solar X-ray spectrum becomes harder and the relative fraction of the total X-ray output at low energies is smaller. Other possible sources of differences in the observed X-ray fluxes between GOES and XFM-CS

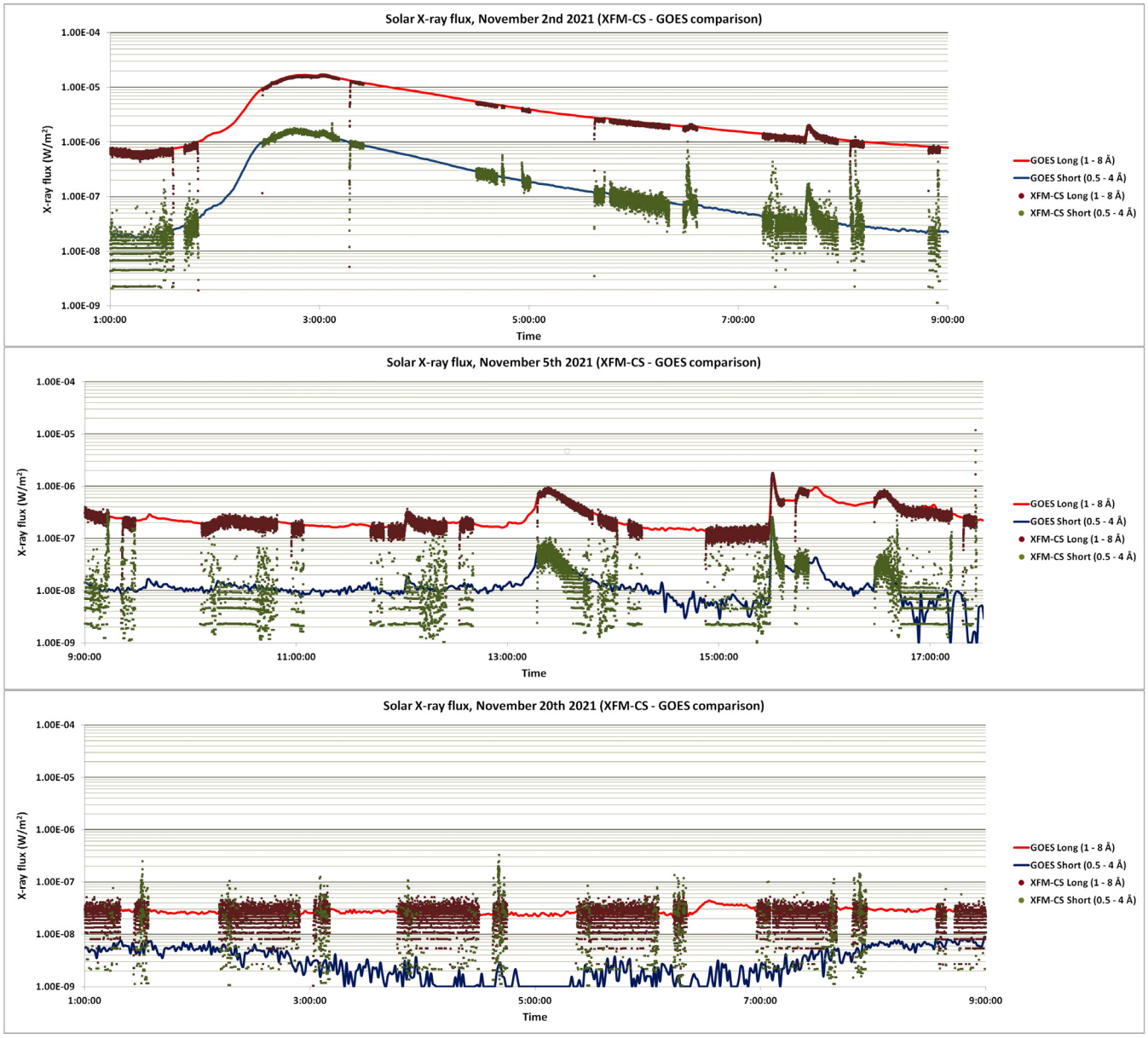

Fig. 22. Comparison between the calibrated solar X-ray flux data measured with XFM-CS and the primary GOES (GOES-16) XRS on November 2 (top), November 5 (middle) and November 20 (bottom) 2021.

include the flux channel bounds of XFM-CS not being compensated for the temperature drift of the energy scale (Section 3.2), and the 60 s nominal measurement cadence of the high-resolution spectral data in XFM-CS, which is longer than some of the fastest changes in the solar X-ray output, in particular during the onset of flares. GOES raw data is obtained with 1 s measurement cadence. In practice, however, neither effect has been identified as sources of any noticeable differences in GOES and XFM-CS fluxes within the energy range of the GOES energy channels.

Fig. 23 also shows that the X-ray fluxes measured with GOES-16 and GOES-17 sometimes differ significantly from each other as well as from the flux measured with XFM-CS, especially in quiescent conditions. This can be clearly seen in the middle and bottom panels of Fig. 23. Electron background causes significant contribution to this difference in all three instruments. GOES XRS data processing pipeline includes correction for electron contamination [8], but the differences in flux values measured with GOES-16 and GOES-17 suggest that this correction is not perfect in situations where X-ray flux is low, electron background is high, and the electron background conditions are different for the two satellites. As noted in Section 4.1, the X-ray fluxes measured with XFM-CS are also affected by the statistical fluctuations of the electron background, particularly at the high energy channels. It should also be noted that the electron environments seen by GOES satellites at geosynchronous orbit and XFM-CS at LEO are in no way comparable with each other due to the presence of Earth's magnetic field and differences in local conditions.

Finally, we investigate a short duration C1 flare, which peaked at 15:30 on November 5 2021. The onset of this flare lasted only about 1 min. The physical X-ray fluxes measured with XFM-CS and both primary and secondary GOES XRS are shown in Fig. 24.

Comparison of the 1 s flux data from XFM-CS with the time averaged 1 min flux data of all three instruments show that the onset of this flare happened so fast that the 60 s moving average smoothened the flux curve and made the rise of the flare look less steep than it actually was. This shows that the 60 s measurement cadence of the high resolution spectrum data of XFM-CS may be too slow for spectroscopic studies of the rapid onset of short duration solar flares. In addition, this is also an additional potential source of error in the calibrated flux data

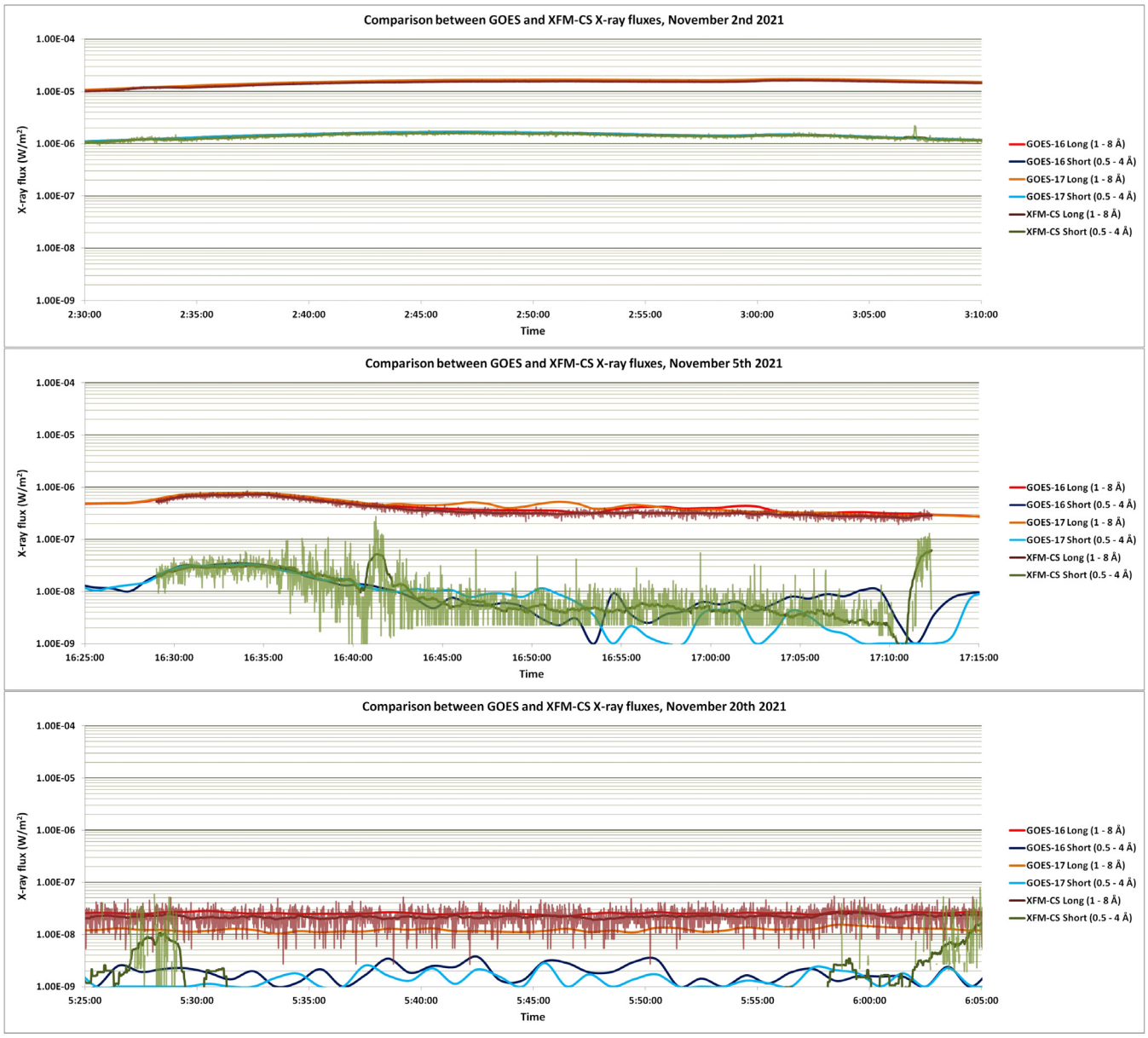

Fig. 23. Comparison between the calibrated solar X-ray flux data measured with XFM-CS and the X-ray sensors of both GOES-16 and GOES-17 on November 2 (top), November 5 (middle) and November 20 (bottom) 2021. The 1 s XFM-CS flux data has been overlaid with 60 s moving average for easier comparison with GOES XRS data.

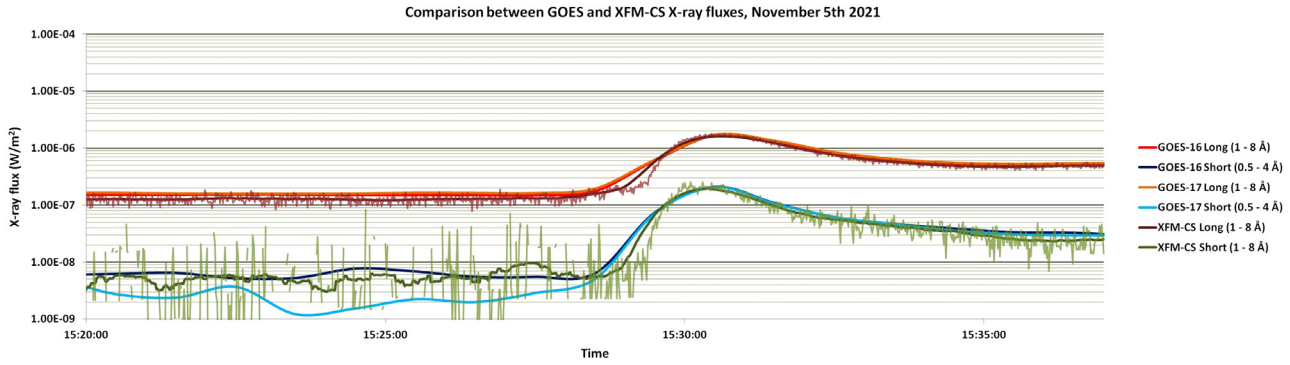

Fig. 24. Comparison of the calibrated solar X-ray flux data measured of a short duration C1 class flare with XFM-CS and the X-ray sensors of both GOES-16 and GOES-17 on November 5 2021. The 1 s XFM-CS flux data has been overlaid with 60 s moving average for easier comparison with GOES XRS data.

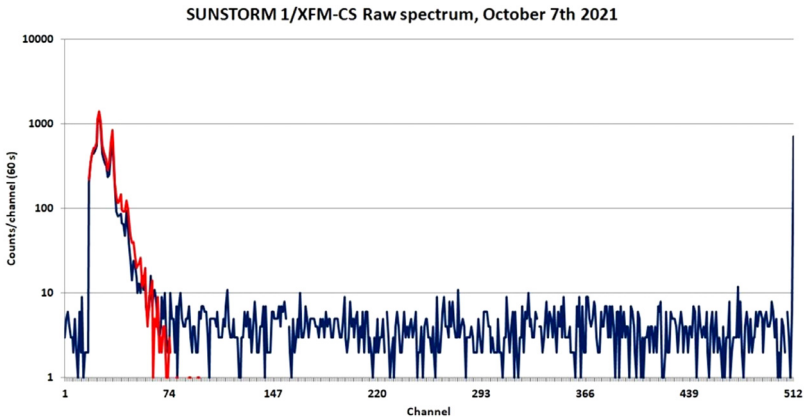

Fig. 25. An example raw spectrum measured with XFM-CS, demonstrating the electron background. The integration start time of the first 60 s spectrum (red) was 13:28:25 (UTC), and it is free of electron contamination. The second spectrum (blue) was measured 5 minutes later beginning at 13:34:25 (UTC), when the S/C was within the edge of the outer radiation belt over the southern latitudes. It contains a moderate level of electron background. The solar X-ray output was relatively low, about $2 \cdot 10^{-7}$ W/m^2 (GOES flux B2).

since the high resolution spectral data is used in the calibration of flux data as part of the science processing pipeline (Section 3.5). Thus, it may be advantageous to change the default measurement cadence of the high resolution spectrum data from 60 s to 16 s, which was the default measurement cadence of the spectral data with the heritage instruments. The drawbacks of this change would include reduced S/N at the lower end of the dynamic range and increased data budget of the instrument.

4.4. Electron background

It has been known since the early operation of the heritage instruments of XFM-CS that solid state detector based solar monitors are sensitive to high energy electron radiation in space. These electrons almost always deposit more energy to the detectors than the upper limit of their energy range, causing them to be counted to the highest integral energy channel. This has been confirmed during the operation of the heritage instruments [24] as well as by Geant4 simulations. However, in XFM-CS the electrons cause an additional flat background throughout the whole spectrum energy range in addition to the expected peak at the highest energy channel. The background also extends below the instrument's low energy threshold. This background was first detected during the in-orbit commissioning of the instrument and was a surprise to the instrument team. We believe that it is caused in the pulse filtering, detection and pulse height analysis process due to the somewhat irregular shape of the raw current pulses caused by electrons within the SDD. The exact cause of this background and its mitigation is currently under investigation by the manufacturer of the read-out electronics of XFM-CS. An example raw spectrum of the electron background measured by XFM-CS during the in-orbit commissioning of the instrument is shown in Fig. 25.

The electron background appears to be completely flat throughout the whole spectrum energy range, and its intensity is directly proportional to the count rate at the highest energy channel. This makes it very easy to identify and filter out during the processing of the science data. The filtering of the electron background has already been implemented into the science processing pipeline of XFM-CS (Section 3.5), but its Poisson statistical fluctuations still cause some noise in particular in the high energy flux channels, where even a small number of counts has significant effect on the flux. The effect was demonstrated in Section 4.1.

Due to its sensitivity to electron radiation, we have also investigated the possibility of using XFM-CS, as well as future XFM instruments for measurement of in-situ electrons. Since XFM instruments do not provide information about the energy spectrum or the directional distribution of the detected electrons, such measurements would be insufficient for meaningful scientific studies of the electron environment. However, the electron flux values have potential value for space weather nowcasts and as confirmation signal of enhancing geomagnetic activity and may be of use also as validation data points for space weather models, especially if the data can be calibrated reliably.

Geant4 simulations were applied to estimate the response of XFM-CS to electrons. Standard electromagnetic physics list option 4, included in the Geant4 distribution, was selected as the set of physics models used in the simulation. The option 4 is considered the most accurate set of electromagnetic physics models available in Geant4 distribution, and it includes accurate models also for the low energy processes in the keV range, which is important for estimating the background signal in thermal X-ray energy range. The electron background was assumed to be dominated by electrons trapped in the Earth's outer radiation belt, and thus AE-8 model was used to approximate their energy spectrum [29]. Finally, the angular distribution of the electron background was assumed to be isotropic. The simulation results show that the minimum energy of electrons that reach the detector's active volume (through the collimator) is >40 keV, and that the sensitivity of XFM-CS to electrons is roughly **1/22500 cm^2 sr**.

The science processing pipeline of XFM-CS (Section 3.5) was updated to also include the electron flux in the calibrated science data. The raw electron counts are divided with the detector's sensitivity to obtain the physical electron flux, which is then combined with the position information of the S/C (latitude, longitude and altitude), forming a dataset of the in-situ electron measurements with XFM-CS. Since the electron flux is derived from the spectrum data, the measurement cadence of the electron flux is the same as that of the high resolution X-ray spectrum data, 60 s by default. An example of the calibrated electron flux data and comparison with data from Polar Operational Environmental Satellites (POES) is shown in Fig. 26. It should also be noted that the accuracy of the electron measurements is quite rough because the actual electron environment can vary significantly over time in both energy spectrum and angular distribution. In addition, the position of the S/C (latitude) will change by ~4° during the 60 s integration time, causing significant changes in the electron environment during the spectrum integration especially at the edge of the outer radiation belt. Thus, the dataset of the electron flux should only be considered approximate. It should, however, be suitable for a trigger signal on increased geomagnetic activity, and possibly as an indicator of enhanced threat level.

5. Discussion and conclusions

SUNSTORM 1 CubeSat was launched to Sun-synchronous low Earth orbit on August 17 2021. The primary purpose of the mission is in-orbit

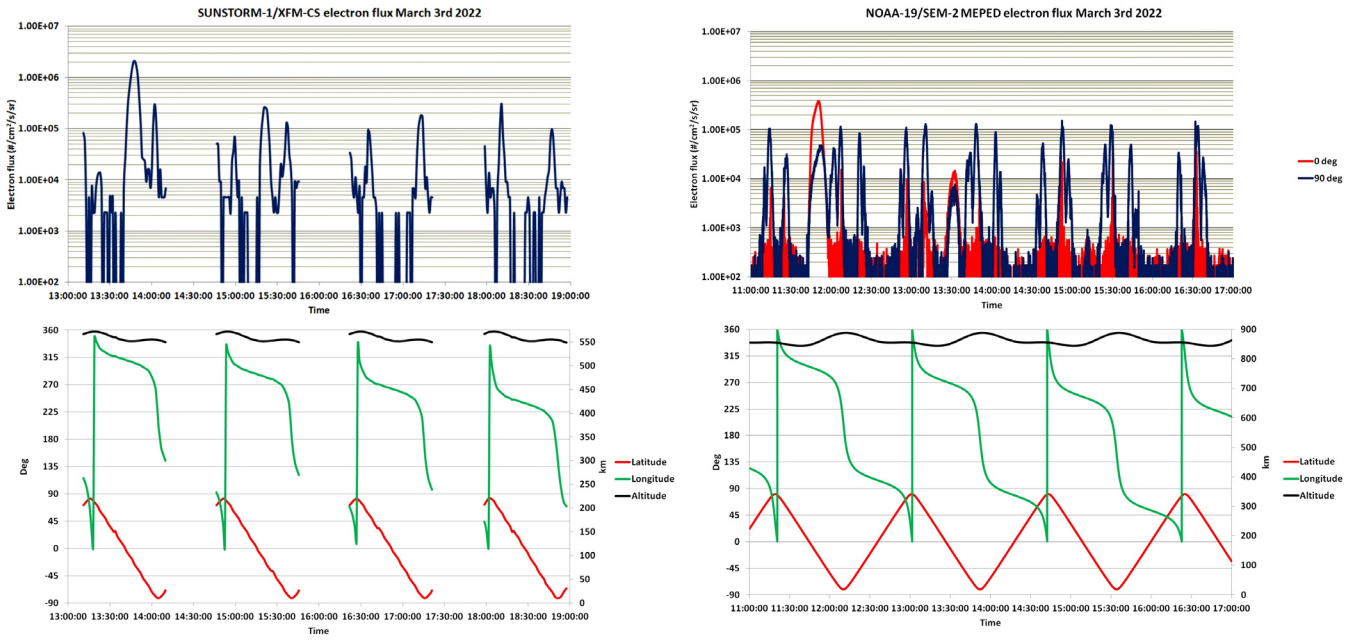

Fig. 26. Comparison between >40 keV electron fluxes measured with SUNSTORM 1/XFM-CS and NOAA-19 Space Environment Monitor 2 (SEM-2) Medium Energy Proton and Electron Detector (MEPED) [30] on March 3 2022. The peak at 11:45 in XFM-CS data and at 13:50 in MEPED data is due to the observing S/C passing through the South Atlantic Anomaly (SAA), a region where the Earth's inner Van Allen radiation belt comes closest to Earth's surface. The relatively high electron flux seen with XFM-CS is due to the SAA fly through occurring near local noon, when the particle density is at its highest.

demonstration of X-ray flux monitor for CubeSats (XFM-CS). XFM is an innovative X-ray spectrometer for observation and characterization of solar flares, which is planned to be used in future space weather services. In the in-orbit commissioning both the S/C and XFM-CS were found to be in good health, and function according to the specifications. The first solar X-ray spectrum was acquired on August 27 2021, i.e. just ten days after the launch. The quality of the data is consistent with the results of the ground characterization of the instrument and meets the scientific requirements.

The design of XFM-CS has heritage from the XSM on-board ESA's SMART-1 [1] and ISRO's Chandrayaan-1 [4] missions to Moon, and the SIXS instrument on-board ESA's and Jaxa's BepiColombo mission to Mercury [7]. XFM-CS is a next generation instrument with improved performance and new technologies for the detector and the electronics. The system has lower electronic noise at any combination of temperature and shaping time as well as improved tolerance to radiation damage, allowing the use of the full potential of the SDD X-ray spectrometer technology, used successfully for the first time in space.

The ground calibrations of the XFM-CS were carried out successfully on September 21–October 6 2020. Due to the similarities of the instruments, especially in the measured data, and main features of the detector front end, the calibration procedures were very similar to those used with the heritage instruments [4,12]. The main difference is the lack of an on-board calibration source in the XFM-CS. In the heritage instruments, on-board calibration sources were used for calibration of the energy scale and energy resolution during the mission between and during observations. With XFM-CS the energy scale and energy resolution were, instead, characterized carefully as functions of temperatures of the read-out electronics and the leakage current, respectively, during the ground calibrations and the results were compiled into look-up tables from which the relevant calibration information is interpolated as part of the science data processing pipeline. This method is considered sufficiently accurate for X-ray flux monitors even though it neglects the possible changes in the calibration of the detector's energy scale or energy resolution from other sources than thermal effects and the leakage current, because such effects have been observed to be minor with the heritage instruments. We have not observed any detectable changes in the energy calibration of XFM-CS during its first five months of operation. However, we still recommend the use of in-flight calibration sources in solid state X-ray sensors for missions where highest possible scientific quality of spectral data is a priority. A summary of the ground calibration results and the values of the key parameters affecting the performance of the instrument are compiled in Table 3 (Section 3.5).

The solar spectrum and flux data obtained with SUNSTORM 1 have demonstrated that the performance of XFM-CS is consistent with the ground calibration results as well as theoretical predictions, indicating that the instrument characterization was successful. The performance of the instrument has been demonstrated with varying levels of solar activity ranging from quiescent to high activity conditions, although at the time of writing this paper we have not yet observed the strongest X-class solar flares. However, a minor thermal effect in the lowest energy flux channel (1.0–1.55 keV) data was detected. The indicated X-ray flux in this channel was observed to increase slightly as the instrument's temperature increases in direct sunlight, and then decrease again during the eclipse periods. The cause of this effect is well understood. It is caused by the combination of the temperature drift of the XFM-CS energy scale, and the minor uncertainties in the thicknesses of the detector materials and filters. The detector's *QE* near its low energy limit is known to be very sensitive to these minor uncertainties. This should be accounted for in the characterization of future XFM instruments.

The calibrated solar X-ray flux values generally closely match the simultaneous GOES observations. GOES Long channel (1–8 Å) flux is usually about 5%–10% higher than the equivalent XFM-CS flux, while GOES Short channel (0.5–4 Å) flux is nearly identical with the equivalent XFM-CS flux during high X-ray flux conditions. The relative difference at low energies also tends to become even smaller during active Sun. We believe that this small difference is caused by the way the channel energy bounds are defined in the two instruments. In GOES XRS detectors the channel energy bounds are defined only by filter transmissions, and thus they have reduced sensitivity also below the nominal channel energies [8], while in XFM-CS the events are distributed into the flux channels in digital domain based on pulse height analysis. The non-zero sensitivity of the GOES XRS detectors

below their nominal energy ranges can explain the slightly higher flux in comparison with XFM-CS. It can also explain why the relative difference becomes smaller as total flux increases, because solar X-ray spectrum is known to become harder as solar activity and plasma temperature increase. We also detected a small uncertainty in the data from both instruments due to electron background. This is most noticeable in the high energy channels during quiescent Sun, but it can sometimes also be detectable at lower energies if the electron background is particularly high.

The data from XFM-CS is essentially free of instrument background, as expected due to the low electronic noise background count rate observed during the ground calibrations. However, during the commissioning of the instrument it was found that high energy electrons in space cause a flat background throughout the whole energy range of the instrument. This was a surprise to the instrument team because the observations made with the heritage instruments as well as Geant4 simulations before launch indicate that practically all electron events deposit more energy to the SDD than the upper limit of the instrument's energy range, and it should therefore be counted into the highest energy channel. The electron background within the spectral energy range is believed to be caused in the pulse filtering process due to the somewhat irregular shape of the current pulses caused by electron events in the SDD. This effect and its mitigation are currently under investigation by the manufacturer of XFM-CS read-out electronics. The science data processing pipeline of XFM-CS was modified by addition of filtering of the electron background. The background is estimated from the number of counts seen in the highest energy channel and then subtracted from the raw spectral and flux data before further processing steps. The filtering is effective, but Poisson statistical fluctuations of the electron background still cause some noise particularly in the high energy flux channels (Channels 5 and 6). Because of this noise we also added a data quality flag into the calibrated solar X-ray flux data, warning about electron contamination during time periods of particularly high electron background.

The possibility for using XFM-CS, as well as future XFM instruments for measurement of in-situ electrons was also investigated. The main source of high energy electrons observed by XFM-CS is the edge of Earth's outer radiation belt. Geant4 simulations were applied to estimate the response of XFM-CS to electrons, using the statistical AE-8 model [29] to approximate the energy spectrum of the trapped electrons, and assuming isotropic angular distribution. The science processing pipeline of XFM-CS was then expanded to include also the physical electron flux in the calibrated science data. The raw electron flux is estimated from the number of counts in the highest energy channel of the spectrum data, which are mostly caused by electrons. XFM-CS was not designed for electron observations, however, and the accuracy of these electron measurements is quite rough, especially since both the energy spectrum and angular distribution are poorly known and the time scale of the changes in the electron flux can be much shorter than the 60 s measurement cadence. Thus, the data of the electron flux should only be considered approximate. However, it is useful as a trigger signal on increased geomagnetic activity, and potentially also for validation of the local space weather model if proper calibration and conversion to physical electron flux can be established.

Conclusively, SUNSTORM 1 mission has successfully demonstrated the applicability and performance of XFM both for monitoring of solar X-ray fluxes and spectra for operative space weather use, and for scientific studies of solar corona.

Declaration of competing interest

The authors declare that they have no known competing financial interests or personal relationships that could have appeared to influence the work reported in this paper.

Acknowledgments

SUNSTORM 1 mission and the development of XFM-CS are funded by ESA within the General Support Technology Programme (GSTP), and Business Finland for supporting the implementation of the project to GSTP (Contract number: 4000122571/17/NL/LF). We would like to express our thanks to everyone in the teams of Isaware Oy, Aboa Space Research Oy, Oxford Instruments Technologies Oy and Talvioja Consulting Oy, who participated in the development of the XFM-CS instrument. Special thanks to the staff of Kuva Space Oy (formerly Reaktor Space Lab Oy) for developing and building the SUNSTORM 1 CubeSat platform as well as for satellite operation and ground station services for the mission. Finally, Finnish Meteorological Institute (FMI) is acknowledged for allowing us to use their facilities during the development and calibrations of XFM-CS.

References

[1] L. Alha, J. Huovelin, T. Hackman, H. Andersson, C.J. Howe, E. Esko, M. Väänänen, The in-flight performance of the X-ray solar monitor (XSM) on-board SMART-1, Nucl. Instrum. Methods A 596 (2008) 317–326.

[2] R.P. Lin, B.R. Dennis, G.J. Hurford, D.M. Smith, A. Zehnder, P.R. Harvey, D.W. Curtis, D. Pankow, P. Turin, M. Bester, A. Csillaghy, M. Lewis, N. Madden, H.F. van Beek, M. Appleby, T. Raudorf, J. McTiernan, R. Ramaty, E. Schmahl, R. Schwartz, S. Krucker, R. Abiad, T. Quinn, P. Berg, M. Hashii, R. Sterling, R. Jackson, R. Pratt, R.D. Campbell, D. Malone, D. Landis, C.P. Barrington-Leigh, S. Slassi-Sennou, C. Cork, D. Clark, D. Amato, L. Orwig, R. Boyle, I.S. Banks, K. Shirey, A.K. Tolbert, D. Zarro, F. Snow, K. Thomsen, R. Henneck, A. Mchedlishvili, P. Ming, M. Fivian, J. Jordan, R. Wanner, J. Crubb, J. Preble, M. Matranga, A. Benz, H. Hudson, R.C. Canfield, G.D. Holman, C. Crannell, T. Kosugi, A.G. Emslie, N. Vilmer, J.C. Brown, C. Johns-Krull, M. Aschwanden, T. Metcalf, A. Conway, The Reuven Ramaty high-energy solar spectroscopic imager (RHESSI), Sol. Phys. 210 (2002) 3–32.

[3] M. Väänänen, L. Alha, J. Huovelin, Cross-calibration of SMART-1 XSM with GOES and RHESSI, Sol. Phys. 260 (2) (2009) 479–488.

[4] L. Alha, J. Huovelin, K. Nygård, H. Andersson, E. Esko, C.J. Howe, B.J. Kellett, S. Narendranath, B.J. Maddison, I.A. Crawford, M. Grande, P. Sreekumar, Ground calibration of the Chandrayaan-1 X-ray solar monitor (XSM), Nucl. Instrum. Methods A 607 (2009) 544–553.

[5] S. Narendranath, P. Sreekumar, L. Alha, K. Sankarasubramanian, J. Huovelin, P.S. Athiray, Elemental abundances in the solar corona as measured by the X-ray solar monitor on-board Chandrayaan-1, Sol. Phys. 289 (5) (2014) 1585–1595.

[6] S. Narendranath, P. Sreekumar, S. Panini, N.S. Pillai, K. Sankarasubramanian, J. Huovelin, Coronal elemental abundances: New results from soft X-ray spectroscopy of the sun, Sol. Phys. 295 (2020) 175.

[7] J. Huovelin, R. Vainio, E. Kilpua, A. Lehtolainen, S. Korpela, E. Esko, K. Muinonen, E. Bunce, A. Martindale, M. Grande, H. Andersson, S. Nenonen, J. Lehti, W. Schmidt, M. Genzer, T. Vihavainen, J. Saari, J. Peltonen, E. Valtonen, M. Talvioja, P. Portin, S. Narendranath, R. Järvinen, T. Okada, A. Milillo, M. Laurenza, E. Heino, P. Oleynik, Solar intensity X-ray and particle spectrometer SIXS: Instrument design and first results, Space Sci. Rev. 2016 (2020) 94.

[8] P.C. Chamberlin, T.N. Woods, F.G. Eparvier, A.R. Jones, Next generation X-ray sensor (XRS) for GOES-R satellite series, in: Proc. SPIE 7438, in: Solar Physics and Space Weather Instrumentation III, vol. 743802, 2009.

[9] W.D. Pesnell, B.J. Thompson, P.C. Chamberlin, The solar dynamics observatory (SDO), Sol. Phys. 275 (1–2) (2012) 3–15.

[10] D. Müller, O.C. St Cyr, I. Zouganelis, H.R. Gilbert, R. Marsden, T. Nieves-Chinchilla, E. Antonucci, F. Auchère, D. Berghmans, T.S. Horbury, R.A. Howard, S. Krucker, M. Maksimovic, C.J. Owen, P. Rochus, J. Rodriguez-Pacheco, M. Romoli, S.K. Solanki, R. Bruno, M. Carlsson, A. Fludra, L. Harra, D.M. Hassler, S. Livi, P. Louarn, H. Peter, U. Schühle, L. Teriaca, J.C. del Toro Iniesta, R.F. Wimmer-Schweingruber, E. Marsch, M. Velli, A. De Groof, A. Walsh, D. Williams, The solar orbiter mission. Science overview, Astron. Astrophys. 642 (A1) (2020) 31.

[11] C. Schlemm, R. Starr, K. Bechtold, S. Hamilton, J. Boldt, W. Boynton, W. Bradley, M. Fraeman, R. Gold, J. Goldsten, J. Hayes, S. Jaskulek, E. Rossano, R. Rumpf, E. Schaefer, K. Strohbehn, R. Shelton, R. Thompson, B. Williams, The X-ray spectrometer on the MESSENGER spacecraft, Space Sci. Rev. 131 (2007) 393–415.

[12] A. Lehtolainen, L. Alha, J. Huovelin, R. Moissl, S. Korpela, H. Andersson, K. Kuparinen, Ground calibrations of the solar intensity X-ray spectrometer (SIXS) on board BepiColombo, Nuclear Instrum. Methods A 735 (2014) 496–511.

[13] B.L. Henke, E.M. Gullikson, J.C. Davis, Atomic data and nuclear data tables, 1993, pp. 181–342, 52 (2).

[14] M.V. Zombeck, Handbook of Space Astronomy and Astrophysics, Experimental Astronomy and Astrophysics, X-Ray and Gamma-Ray Detectors, second ed., Cambridge University Press, 1990, pp. 358–369, (Chapter 14).

[15] L. Strüder, G. Lutz, P. Lechner, H. Soltau, P. Holl, X-Ray Spectrometry: Recent Technological Advances, X-Ray Detectors, Wiley, 2004, pp. 133–275, (Chapter 4).
[16] G.W. Phillips, K.W. Marlow, Automatic analysis of gamma-ray spectra from germanium detectors, Nucl. Instrum. Methods 137 (3) (1976) 525–536.
[17] A. Vasilescu, G. Lindström, Displacement damage in silicon, 2000, https://rd50.web.cern.ch/rd50/NIEL/default.html. (Accessed 7 February 2022).
[18] H.S. Hudson, Solar flares, microflares, nanoflares and coronal heating, Sol. Phys. 133 (2) (1991) 357–369.
[19] J.A. Klimchuk, Nanoflare heating: Observations and theory, 2017, arXiv e-prints, arXiv:1709.07320.
[20] B. Mondal, A. Sarkar, S.V. Vadawale, N.P.S. Mithun, P. Janardhan, G. Del Zanna, H.E. Mason, U. Mitra-Kraev, S. Narendranath, Evolution of elemental abundances during B-class solar flares: Soft X-ray spectral measurements with chandrayaan-2 XSM, Agron. J. 920 (2021) 1.
[21] J.M. Laming, The FIP and inverse FIP effects in solar and stellar Coronae, Living Rev. Sol. Phys. 12 (2015) 2.
[22] J.M. Laming, The FIP and inverse FIP effects in solar flares, Agron. J. 909 (1) (2021) 17.
[23] K.A. Arnaud, in: G. Jacoby, J. Barnes (Eds.), Astronomical Data Analysis Software and Systems V, in: ASP Conference Series, vol. 101, 1996, p. 17.
[24] M. Uunila, Investigations of Particle Detection Capability of the XSM on SMART-1 (M.Sc.-thesis), University of Helsinki, 2007.
[25] B. AtomD, Atomic data for astrophysicists, 2022, http://www.atomdb.org/index.php. (Accessed 7 February 2022).
[26] E. Antonucci, B.R. Dennis, A.H. Gabriel, G.M. Simnett, Initial phase of chromospheric evaporation in a solar flare, Sol. Phys. 96 (1) (1985) 129–142.
[27] T. Yokoyama, K. Shibata, A two-dimensional magnetohydrodynamic simulation of chromospheric evaporation in a solar flare based on a magnetic reconnection model, Agron. J. 494 (1998) L113–L116.
[28] A. Czaykowska, B.D. Pontieu, D. Alexander, G. Rank, Evidence for chromospheric evaporation in the late gradual flare phase from SOHO observations, Agron. J. 521 (1) (1999) L75–L78.
[29] J.I. Vette, The AE-8 Trapped Electron Model Environment, NSSDC/WDC-A-R & S Report 91-24, NASA-GSFC, 1991.
[30] D.S. Evans, M.S. Greer, Polar orbiting environmental satellite space environment monitor - 2 instrument descriptions and archive data documentation, 2004, NOAA Technical Memorandum OAR SEC 93, version 1.4.